AN ABSTRACT OF THE THESIS OF

Lei Jin for the degree of Master of Science in Electrical and Computer Engineering presented on March 13, 2015.

Title: DC Bus Capacitor Discharge of Permanent Magnet Synchronous Machine Drive Systems for Hybrid/Electric Vehicles

Abstract approved:

_____

Julia Zhang Ted K.A. Brekken

Permanent magnet synchronous machines (PMSMs) are widely used in electric vehicles and hybrid electric vehicles to propel the wheels. Various control strategies have been developed for PMSM drive systems to achieve both high efficiency and safe operation. In a PMSM drive system, generally the high voltage battery and the power converters are connected by a relay. In vehicle key-off events, although the battery is isolated immediately from the relay, the DC bus filter capacitor has to be discharged as quickly as possible to avoid an electrical hazard. This research explores the DC bus capacitor discharge of PMSM drive systems for hybrid/electric vehicles. Based on analyzing the power flow during discharge, a three-stage discharge algorithm has been developed, including a fast discharge stage, a DC bus voltage closed-loop regulation stage, and an inverter shutdown stage. The DC bus capacitor is quickly and safely discharged by dynamically adjusting the command currents for the current vector control of PMSMs. Both simulation and experimental results show the feasibility and performance of the proposed discharge technique.

DC Bus Capacitor Discharge of Permanent Magnet Synchronous Machine Drive Systems for Hybrid/Electric Vehicles

by
Lei Jin

A THESIS

submitted to

Oregon State University

in partial fulfillment of
the requirements for the
degree of

Master of Science

Presented March 13, 2015
Commencement June 2015

Master of Science thesis of Lei Jin presented on March 13, 2015

APPROVED:

Major Professor, representing Electrical and Computer Engineering

Director of the School of Electrical Engineering and Computer Science

Dean of the Graduate School

I understand that my thesis will become part of the permanent collection of Oregon State University libraries. My signature below authorizes release of my thesis to any reader upon request.

Lei Jin, Author

ACKNOWLEDGEMENTS

I would first like to thank my advisor, Dr. Julia Zhang, for providing me the opportunity to study in the U.S. and for her guidance and motivation. Her diligence, attention to details, and pursuit for perfection have inspired me throughout my research and will continue motivating me in the future. I would also like to thank Dr. Ted Brekken and Dr. Xiaolin Wang for co-advising me on part of my research. Their deep expertise and gracious manners have kept reminding me that while cleverness is a given gift, kindness is a choice hard to make. Thank you also to Dr. Annette von Jouanne and Dr. Karl R. Haapala for being part of my committee.

I would like to thank Mike Starrett, Han Xiong, and Kaushal Kb for their unforgettable spiritual company through interest in humor, arts and math, and philosophy. I am also deeply grateful to Jiajia Song for his sincere friendship throughout my graduate study. Thank you to all the other friends, both inside and outside the energy system group, for making me a better person.

Thank you to Ford Motor Company for the financial support and technical advice. This work would never reach so far without the research funding provided and background developed there.

And finally I must thank my family in China for all their support and encouragement. Thank my father for striving for the best possible education for me.

TABLE OF CONTENTS

TABLE OF CONTENTS (Continued)

LIST OF FIGURES

LIST OF FIGURES (Continued)

Figure Page

LIST OF FIGURES (Continued)

Figure Page

LIST OF TABLES

DC Bus Capacitor Discharge of Permanent Magnet Synchronous Machine Drive Systems for Hybrid/Electric Vehicles

1 Introduction

In recent years, hybrid/electric vehicles have attracted increasing interest in the world as an alternative to traditional combustion engine vehicles due to their high energy efficiency and environmental friendliness. Governments around the world have made policies to offer financial incentives for consumers buying them [2], [3]. Automotive companies, both industry incumbents such as General Motors and Toyota and newcomers like Tesla Motors, have made major investments in electric vehicle (EV) technology. Consumers are also changing their attitudes towards EVs rapidly. Figure 1.1 shows the dramatic increase of EV sales in the U.S. from 2010 to 2014 [1].

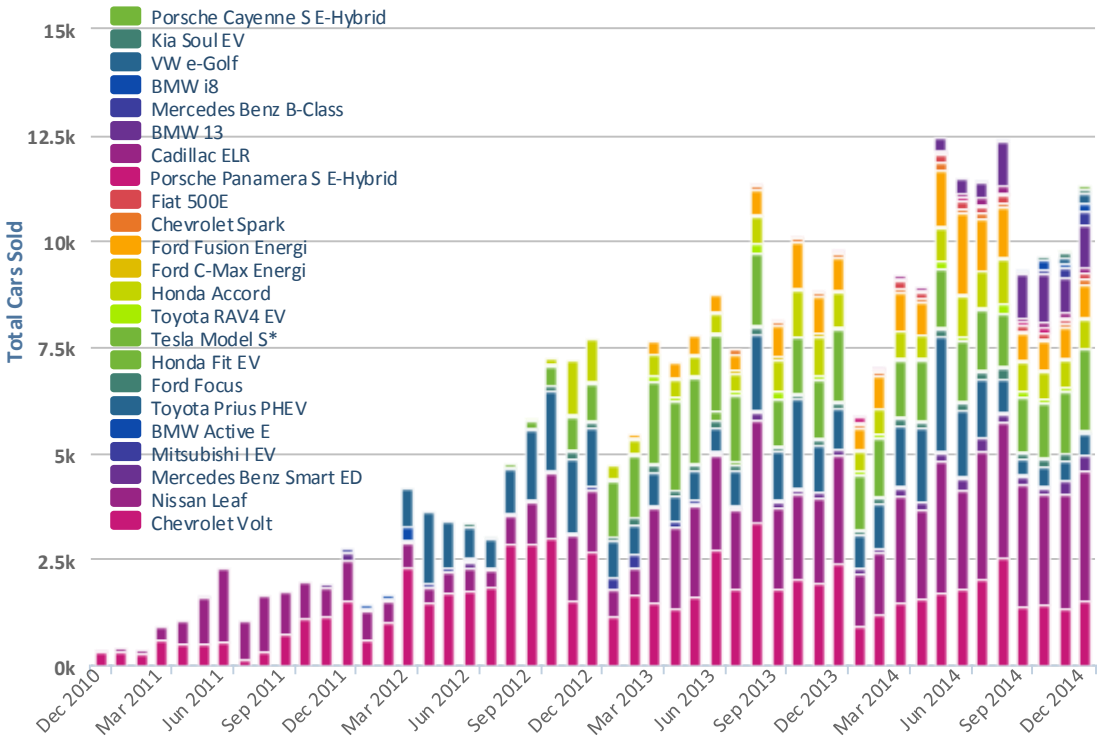

Figure 1.1. Monthly electric vehicle sales in the U.S. (data updated 1/20/2015)

Typically, electric vehicles can be divided into battery electric vehicles (BEVs), hybrid electric vehicles (HEVs) and fuel cell electric vehicles (FCVs), depending on their energy sources and powertrain structures. A BEV is powered by a battery pack (or an ultra-capacitor) alone and converts stored electrical energy into mechanical energy through an electric machine that drives the wheels. An HEV uses both an internal combustion engine (ICE) and one or more electric machines. The ICE uses combustion to convert chemical energy stored in gasoline (or diesel) into mechanical energy, which is then used to drive either the electric machine (in a series HEV) or the wheels together with the electric machine (in a parallel HEV) [4]. An FCV generates electricity from the hydrogen stored in fuel cells and then uses it to either drive the electric machine or charge the battery (or ultra-capacitor). The three categories of EVs are compared at length in Table 1.1 on the basis of their propulsion devices, energy sources, crude oil dependence, drive ranges, and commercial availability [5]. The Toyota Mirai FCV was just released in Japan in December 2014 [6].

Table 1.1 Characteristics of BEVs, HEVs and FCVs

	Types of EVs		
	BEVs	**HEVs**	**FCVs**
Energy sources	Battery/ ultra-capacitor	ICE Battery/ultra-capacitor	Fuel cells Battery/ ultra-capacitor
Propulsion	Electric machines	ICE & Electric machines	Electric machines
Dependence on crude oils	Independent	Dependent	Independent
Driving range	Relatively short	Long	Satisfied
Availability	Commercially available	Commercially available	Under development

Despite the differences above, notice from Table 1.1 that all the hybrid/electric vehicles are partly or fully propelled by one or more electric machines. In fact, the overall performance of a hybrid/electric vehicle is highly dependent on its electric machine drive system. The electric machine drive system is one of the key contributors to the overall higher efficiency and lower emissions of hybrid/electric vehicles compared to those ICE powered vehicles [7]. This chapter will first introduce the electric machine drive systems in hybrid/electric vehicles, then discuss one of the issues in the electric machine drive systems, which motivated this research work, and finally generalize the scope of this thesis.

1.1 Electric Machine Drive Systems in hybrid/electric vehicles

As shown in Figure 1.2, the electric machine drive system in a hybrid/electric vehicle typically consists of the electric machine, the power converter, the controller and the sensing system including the voltage, current, and rotor position sensors [8]. The power converter contains power switches that can be cycled on and off to produce AC voltages of variable magnitudes and frequencies to the AC electric machine. This enables the electric machine to be operated at a specific desired speed and torque. The controller generates the needed switching signals for the power converter based on the current, voltage, position and speed of the AC electric machine.

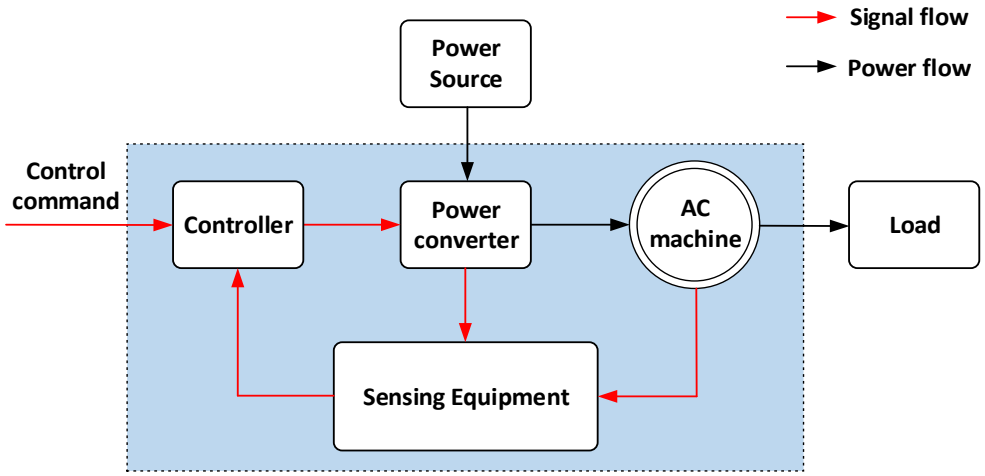

Figure 1.2. Block diagram of electric machine drive systems in hybrid/electric vehicles

The electric machine drive systems are designed such that the electric machine can work in both motoring mode and generating mode. When motoring, it converts the stored electrical energy in the battery into mechanical energy and outputs positive torque to drive the wheels. When generating, it recycles the mechanical energy from the wheels and converts it into electrical energy that charges the battery, which is also called regenerative braking. The bi-directional power flow between the battery and electric machine is managed by the power converter with a typical topology as shown in Figure 1.3.

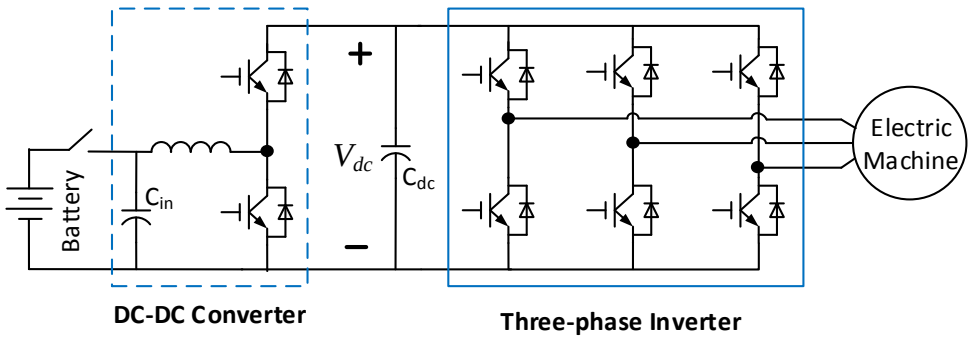

Figure 1.3. Topology of power converter(s) in EV electric machine drive systems

The three-phase inverter is used to convert the DC voltage of the battery into AC voltage that drives the electric machine and is always required. Hard switching is widely used in the three-phase inverter for most commercially available EV products [8]. A DC-DC converter may be used between the battery and the inverter to increase (boost) the battery voltage to provide extended speed capability for the electric machine and optimize the efficiency of the entire electric machine drive system.

There are three typical types of electric machines that can be used in EV electric machine drive systems: 1) permanent magnet (PM) synchronous machines; 2) induction machines; and 3) switched reluctance machines [5]. PM machines, although expensive, have become the most common type of electric machine used in hybrid/electric vehicles because of their high power density and efficiency. Beyond their cost, PM machines also suffer from high eddy-current losses when operating in field-weakening area at high speeds, and the inherent back electromotive force (back EMF) generated by the PM can be very problematic in a case of inverter turnoff due to system fault. The latter issue is the focus of this research presented later in this thesis.

Induction machines are also used in EV powertrains, e.g. Tesla model S, due to their high starting toque, low cost, high reliability and wide availability [9]. An induction machine can be completely de-energized by turning off all the power electronic switches if there is such a need under high speed operation, i.e. a machine fault requires a system shut-down. But on the other hand, the inherent rotor loss makes induction machines generally less efficient than PM machines.

Switched reluctance machines are emerging as a new choice for EV electric machine drive systems. They are fault tolerant and highly reliable due to the magnetic and electric independence between phases [8]. The simple and rugged structure allows them to work in high temperatures and speeds. However, they also produce more noise and larger torque ripple than the other two types of electric machines.

1.2 Research Motivations

Due to the significant role of the EV electric machine drive systems, various control methodologies have been developed to assure not only its high-efficiency operation but also its safe shutdown. In a key-off event, the battery and the power converter in the electric machine drive system will be disconnected immediately by a relay to suspend the power source and protect the battery (see in Figure 1.4). Meanwhile, the rotary shaft of the electric machine will be decoupled from the gear mechanism [10], making the electric machine run with zero load and thus remain high speeds for a relatively long time due to the mechanical inertia. In this situation, if a PM synchronous machine (PMSM) is used for propulsion, which is the case for most hybrid/electric vehicles, the inherent back EMF voltage can remain high for a relatively long time. This high voltage can turn on the inverter diodes and cause current to charge the DC bus capacitor (C_{dc}), even if all the insulated gate bipolar transistors (IGBTs) are turned off. As a result, it can take a long time to drop the DC bus voltage to a safe level. This enduringly high DC bus voltage can be a significant hazard to the persons in the vehicle.

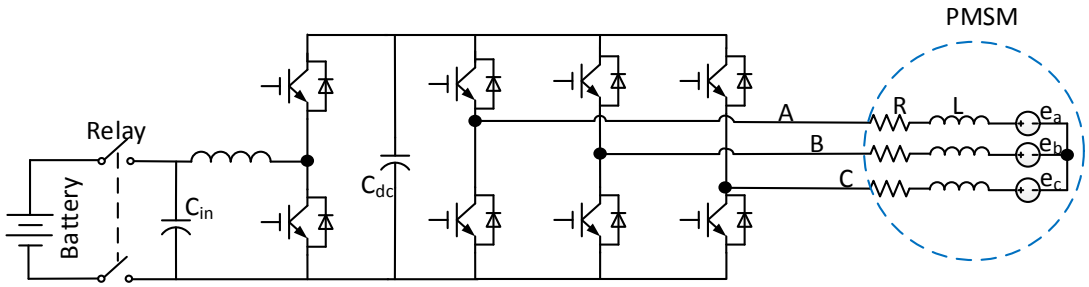

Figure 1.4. Relay connecting battery and PMSM drive system

A conventional solution to reduce DC bus voltage is to add a brake chopper unit in parallel with the dc bus capacitor. During vehicle fault, the excessive energy on the capacitor can be dissipated by the resistor in the chopper circuit. An even simpler method is to turn on either the three upper IGBTs or the three bottom IGBTs of the inverter simultaneously when the relay is disconnected [21]. This method avoids the impact of the back EMF by shorting the electric machine terminals. However, this method can cause a dramatic increase of current in the inverter. Previous research towards an improved strategy proposes a solution with a two-stage control: firstly, control the switching patterns to charge and discharge the bus capacitor and ensure a zero *q*-axis current; secondly, short the electric machine terminals [10]. Although this method was only used to suppress the rising DC bus voltage instead of decreasing it to a safe level, it indicates that the DC bus voltage can be held at a certain level by controlling the *q*-axis current to charge and discharge the DC bus capacitor. The research presented in this thesis aims to look into the interconnection between the dc bus capacitor discharge and the *d*-axis and *q*-axis currents. Based on the existing current vector control theory of PM synchronous machines, this research develops a new current control algorithm that discharges the DC bus capacitor in a relatively short

time, so that the entire electric machine drive system can be shut down quickly in a key-off event.

1.3 Scope of Thesis

The primary objective of this thesis is to explore if a novel scheme to dynamically control the PMSM stator current can be used to quickly discharge the DC bus capacitor of PMSM drive systems for hybrid/electric vehicles after the battery has been disconnected. In describing this research, it is necessary to first introduce the fundamentals of PM synchronous machine drive, including the theory of reference frame transformation, the voltage and torque equations of PMSMs in the *dq* rotating reference frame, and several typical control algorithms of PMSMs.

After detailing the basic operating principles of PMSM drive systems, the DC bus capacitor discharge problem is analyzed. This includes a discussion of several existing potential solutions along with each of their respective shortcomings. A new DC bus capacitor discharge algorithm for PM synchronous machine drive systems is then proposed based on the analysis of system power flow during discharge. Two methods are developed for the DC bus voltage closed-loop regulation during discharge.

Both computer simulations and experimental tests are carried out to examine the feasibility of the proposed discharge algorithm. Part of the modeling work in Simulink/MATLAB are explained and the simulation results are shown and analyzed. The hardware and software used for the experimental verification are presented, with the experimental results discussed at length.

During the experimental testing, the back EMF voltage is found to carry relatively large amount of harmonics. In order to better regulate the PMSM stator current for the DC bus capacitor discharge, a back EMF harmonic compensation algorithm is implemented to compensate the effect of the inherent back EMF harmonics. This algorithm is presented at the end of this thesis with both simulation and experimental results.

2 Fundamentals of PM Synchronous Machine Drive

In this chapter, the voltage equations of PM synchronous machines in the synchronous reference frame are presented based on the theory of reference frame transformation. Then voltage operation limit of PM synchronous machines is analyzed to show the necessity of field weakening operation. The classic current closed-loop control and speed closed-loop control of PM synchronous machines are reviewed. In the end, two improved forms of current regulator with decoupling are introduced for surface PMSMs using complex vector modeling and interior PMSMs using transfer matrix modeling.

2.1 Theory of Reference Frame Transformation

For an ideal AC electric machine, the voltage, current and flux linkage in each phase are changing sinusoidally with time to produce a magnetic field that has a sinusoidal distribution and rotates at a constant speed in the air gap. Moreover, for an interior PMSM, the inductances of its stator windings are also changing sinusoidally with the rotor position angle. In practice, it is too time-consuming to analyze and solve the time-variant differential equations of its mathematical modeling. Therefore, the theory of reference frame transformation is built based on the theory of space vector to simplify the modeling and analysis of AC electric machines.

2.1.1 Theory of Space Vector

The space vector theory is widely applied in AC electric machine drive systems to analyze the three-phase changing quantities in a form of complex vector in space. The

space vector theory is based on the assumption that each phase winding produces a sinusoidal flux density in the air gap [13], [14]. For a three-phase two-pole electric machine, the current direction and winding distribution are illustrated in Figure 2.1. If a magnetic axis is defined for Phase A at the location where its maximum magnetic motive force (MMF) appears, then the MMF in the air gap produced by Phase A current alone is [13]:

$$F_a = \frac{N_s}{2} i_a \cos(\delta) \tag{2.1}$$

where δ is an arbitrary angle that is spatially away from A-axis (see in Figure 2.1 (a)); N_s is the number of turns of each phase winding. Since Phase B and Phase C windings are spatially displaced from Phase A by 120 electrical degrees, their magnetic axes are similarly defined in Figure 2.1 (b) and (c), with the air-gap MMFs produced by them written as:

$$F_b = \frac{N_s}{2} i_b \cos\left(\delta - \frac{2\pi}{3}\right) \tag{2.2}$$

$$F_c = \frac{N_s}{2} i_c \cos\left(\delta + \frac{2\pi}{3}\right) \tag{2.3}$$

Therefore, the total air-gap MMF at angle δ resulting from all the stator phase currents is:

$$F_s = \frac{N_s}{2}\left[i_a \cos(\delta) + i_b \cos\left(\delta - \frac{2\pi}{3}\right) + i_c \cos\left(\delta + \frac{2\pi}{3}\right)\right] \tag{2.4}$$

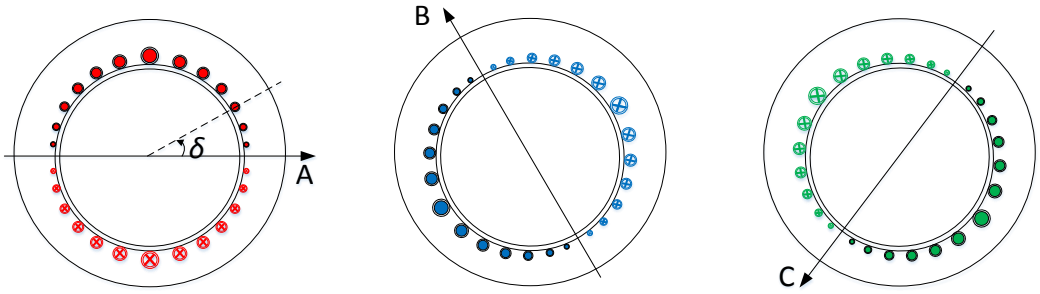

(a) Phase A (b) Phase B (c) Phase C

Figure 2.1. Magnetic axis of each phase winding (each phase produces a sinusoidal flux density in the air gap)

Notice that the total MMF is a function of both space angle δ and time t. A complex plane is defined with the real axis aligned with the predefined A-axis (see in Figure 2.2). Then the time-varying phase currents can be represented by the following vectors:

$$\boldsymbol{I_a} = i_a(t)e^0 \tag{2.5}$$

$$\boldsymbol{I_b} = i_b(t)e^{2\pi/3} \tag{2.6}$$

$$\boldsymbol{I_c} = i_c(t)e^{-2\pi/3} \tag{2.7}$$

Furthermore, a unit vector is defined to represent the spatial position angle δ:

$$\boldsymbol{e_\delta} = cos\delta + jsin\delta \tag{2.8}$$

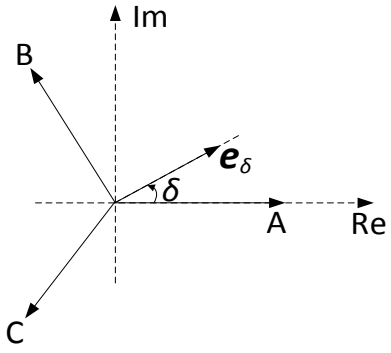

Figure 2.2. Vectors defined in the complex plane.

Then the total MMF in the air gap can be rewritten into:

$$F_s = \frac{N_s}{2}(\boldsymbol{I_a}\cdot\boldsymbol{e_\delta} + \boldsymbol{I_b}\cdot\boldsymbol{e_\delta} + \boldsymbol{I_c}\cdot\boldsymbol{e_\delta}) = \frac{N_s}{2}(\boldsymbol{I_a} + \boldsymbol{I_b} + \boldsymbol{I_c})\cdot\boldsymbol{e_\delta} \tag{2.9}$$

where '·' denotes the dot product between two vectors. It can be seen that the MMF in the air gap can be completely determined by the vector ($\boldsymbol{I_a}$+$\boldsymbol{I_b}$+$\boldsymbol{I_c}$), which is a time-varying vector in the stationary complex plane. Therefore, in practice, we define a current *space vector* in the following manner:

$$\boldsymbol{I_s} = \frac{2}{3}(\boldsymbol{I_a} + \boldsymbol{I_b} + \boldsymbol{I_c}) = \frac{2}{3}(i_A + i_B e^{\frac{2\pi}{3}} + i_C e^{-\frac{2\pi}{3}}) \tag{2.10}$$

Accordingly,

$$F_s = \frac{3N_s}{4}\boldsymbol{I_s}\cdot\boldsymbol{e_\delta} \tag{2.11}$$

Quantities defined in the manner of (2.10) are called ***space vectors***. Likewise, the voltage space vector and the flux linkage space vector are calculated from the three-phase voltage and three-phase flux linkage. It can be proven that for any three-phase balanced sinusoidal quantity, the corresponding space vector has a constant magnitude and rotates at a constant angular velocity in the complex plane.

The space vector theory enables the representation of a three-phase quantity (current, voltage, or flux linkage) by a single rotating vector in the complex plane. The representation of a space vector can be simplified by transforming it into a time-invariant orthogonal coordinate system. It often takes two steps to complete this transformation—Clarke transformation and Park transformation.

2.1.2 **Clarke Transformation**

In Figure 2.3, a space vector $\boldsymbol{f}$ is composed by its three phase quantities $\boldsymbol{f_a}$, $\boldsymbol{f_b}$ and $\boldsymbol{f_c}$ in the form of (2.10). Notice that it is straightforward to represent a vector by its real part and imaginary part. Therefore, a stationary $\alpha\beta 0$ reference frame is built in the same complex plane. The α-axis and β-axis components are calculated from the real parts and the imaginary parts of complex vectors as follows:

$$f_\alpha = Re(\boldsymbol{f}) = Re\left[\frac{2}{3}(\boldsymbol{f_a} + \boldsymbol{f_b} + \boldsymbol{f_c})\right] = \frac{2}{3}[Re(\boldsymbol{f_a}) + Re(\boldsymbol{f_b}) + Re(\boldsymbol{f_c})]$$
$$= \frac{2}{3}\left(f_a - \frac{1}{2}f_b - \frac{1}{2}f_c\right) \quad (2.12)$$

$$f_\beta = Im(\boldsymbol{f}) = Im\left[\frac{2}{3}(\boldsymbol{f_a} + \boldsymbol{f_b} + \boldsymbol{f_c})\right] = \frac{2}{3}[Im(\boldsymbol{f_a}) + Im(\boldsymbol{f_b}) + Im(\boldsymbol{f_c})]$$
$$= \frac{2}{3}\left(0 + \frac{\sqrt{3}}{2}f_b - \frac{\sqrt{3}}{2}f_c\right) \quad (2.13)$$

A virtual axis, 0-axis, is added to take into account the zero-sequence component and make the transformation reversible. As a result, the transformation in the stationary reference frame is written as:

$$\begin{bmatrix} f_\alpha \\ f_\beta \\ f_0 \end{bmatrix} = \frac{2}{3}\begin{bmatrix} 1 & -1/2 & -1/2 \\ 0 & \sqrt{3}/2 & -\sqrt{3}/2 \\ 1/2 & 1/2 & 1/2 \end{bmatrix}\begin{bmatrix} f_a \\ f_b \\ f_c \end{bmatrix} \quad (2.14)$$

which is called the Clarke transformation. Its inverse transformation is:

$$\begin{bmatrix} f_a \\ f_b \\ f_c \end{bmatrix} = \begin{bmatrix} 1 & 0 & 1 \\ -1/2 & \sqrt{3}/2 & 1 \\ -1/2 & -\sqrt{3}/2 & 1 \end{bmatrix}\begin{bmatrix} f_\alpha \\ f_\beta \\ f_0 \end{bmatrix} \quad (2.15)$$

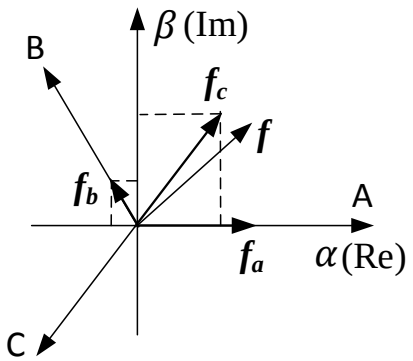

Figure 2.3. Clarke transformation in the $\alpha\beta 0$ stationary reference frame.

With the Clarke transformation, a space vector can always be uniquely represented by its α-axis and β-axis components. However, these two components are still changing sinusoidally. The *dq* rotating reference frame is introduced next to further simplify the representation of the space vector.

2.1.3 **Park Transformation**

In Figure 2.4, a *dq* reference frame is defined to rotate at the same speed as the space vector $\boldsymbol{f}$. The *d*-axis is leading the α-axis by an electrical angle of θ_e, and the *q*-axis is leading the *d*-axis by 90 electrical degrees. The transformation from the $\alpha\beta 0$ stationary reference frame to the $dq0$ rotating reference frame is:

$$\begin{bmatrix} f_d \\ f_q \end{bmatrix} = \begin{bmatrix} cos\theta_e & sin\theta_e \\ -sin\theta_e & cos\theta_e \end{bmatrix} \begin{bmatrix} f_\alpha \\ f_\beta \end{bmatrix} \tag{2.16}$$

which is called the Park transformation. By calculating the inverse of the transformation matrix above, the inverse Park transformation can be obtained as:

$$\begin{bmatrix} f_\alpha \\ f_\beta \end{bmatrix} = \begin{bmatrix} cos\theta_e & -sin\theta_e \\ sin\theta_e & cos\theta_e \end{bmatrix} \begin{bmatrix} f_d \\ f_q \end{bmatrix} \tag{2.17}$$

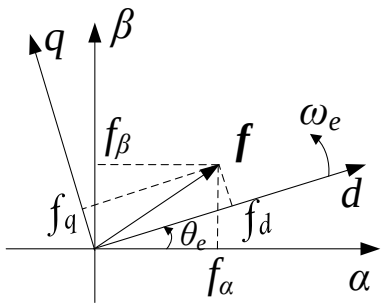

Figure 2.4. Park transformation from the *αβ0* stationary reference frame to the *dq*0 rotating reference frame.

For a three-phase sinusoidal quantity ($f_a+f_b+f_c=0$), the corresponding space vector is standstill in the *dq* rotating reference frame. Hence, its *d*-axis and *q*-axis components become constants. For a PM synchronous machine, the *d*-axis is often aligned with the north pole of the magnets and *q*-axis leading the *d*-axis by 90 electrical degrees. Since the PM on the rotor is rotating synchronously with the space vector, all the quantities (current, voltage and flux linkage) can be easily controlled in the *dq* rotating reference frame.

2.2 Field Weakening Operation of PM Synchronous Machines

2.2.1 Voltage Operation Limit of PM Synchronous Machines

For a PM synchronous machine, the rotor is naturally excited by the permanent magnet, and the stator is excited by the three-phase current. The stator three-phase voltage in the stationary reference frame can be written as:

$$\begin{bmatrix} V_{as} \\ V_{bs} \\ V_{cs} \end{bmatrix} = R_s \begin{bmatrix} i_{as} \\ i_{bs} \\ i_{cs} \end{bmatrix} + p \begin{bmatrix} \lambda_{as} \\ \lambda_{bs} \\ \lambda_{cs} \end{bmatrix} \tag{2.18}$$

where V_{as}, V_{bs} and V_{cs} are the three phase voltages; i_{as}, i_{bs} and i_{cs} are the three phase currents; λ_{as}, λ_{bs}, and λ_{cs} are the phase flux linkages seen by the stator windings; R_s is the resistance of the phase winding; p is the derivative operator, d/dt.

Notice that the phase flux linkages above are produced by both the phase currents and the PM. After applying the stationery to rotating reference frame transformation, the voltage equations in the dq rotating reference frame are written as [15]:

$$\begin{bmatrix} V_d \\ V_q \end{bmatrix} = \begin{bmatrix} R_s & -\omega_e L_q \\ \omega_e L_d & R_s \end{bmatrix} \begin{bmatrix} i_d \\ i_q \end{bmatrix} + \begin{bmatrix} L_d & 0 \\ 0 & L_q \end{bmatrix} p \begin{bmatrix} i_d \\ i_q \end{bmatrix} + \begin{bmatrix} 0 \\ \omega_e \lambda_m \end{bmatrix} \tag{2.19}$$

where V_d and V_q are the d-axis and q-axis voltages, i_d and i_q the d-axis and q-axis currents, L_d and L_q the d-axis and q-axis inductances, ω_e the electrical angular velocity, λ_m the flux linkage of the permanent magnet.

Due to the limited DC bus voltage, there is a maximum phase voltage the inverter can supply to the PM synchronous machine. The voltage utilization in the inverter is described by the modulation index:

$$m = \frac{V_{1m}}{\frac{1}{2} V_{dc}} \tag{2.20}$$

where V_{dc} is the DC bus voltage; V_{1m} is the magnitude of the fundamental phase voltage output to the electric machine. When the space vector PWM (SVPWM) technique is used for the three-phase inverter, the fundamental phase voltage available in linear modulation range is limited by [16], [17]:

$$V_{1m} \leq \frac{V_{dc}}{\sqrt{3}} \tag{2.21}$$

which results in the largest modulation index of $2/\sqrt{3}\approx1.15$. It also imposes a voltage limit for V_d and V_q as:

$$V_d^2 + V_q^2 = V_{1m}^2 \leq \frac{V_{dc}^2}{3} \tag{2.22}$$

The voltage limit above is often analyzed in the i_d-i_q plane to examine its impact on the operation of the electric machine. The analysis often assumes a steady-state operation and a small voltage drop across the winding resistance that can be ignored. Therefore, (2.19) can be rewritten into:

$$\begin{bmatrix} V_d \\ V_q \end{bmatrix} = \begin{bmatrix} 0 & -\omega_e L_q \\ \omega_e L_d & 0 \end{bmatrix} \begin{bmatrix} i_d \\ i_q \end{bmatrix} + \begin{bmatrix} 0 \\ \omega_e \lambda_m \end{bmatrix} \tag{2.23}$$

Substituting (2.23) into (2.22), we can get:

$$(\lambda_m + L_d i_d)^2 + \left(L_q i_q\right)^2 \leq \frac{V_{dc}^2}{3\omega_e^2} \tag{2.24}$$

Under a specific machine speed and DC bus voltage, the voltage limit curve in the i_d-i_q plane is a closed circle for a surface PM synchronous machine (L_d=L_q) or a closed ellipse for an interior PM synchronous machines ($L_d \neq L_q$). The center of the circle or the ellipse always lies at ($-\lambda_m/L_d$, 0). Figure 2.5 illustrates the voltage limits of an interior PM synchronous machine under two different ratios of DC bus voltage and machine speed.

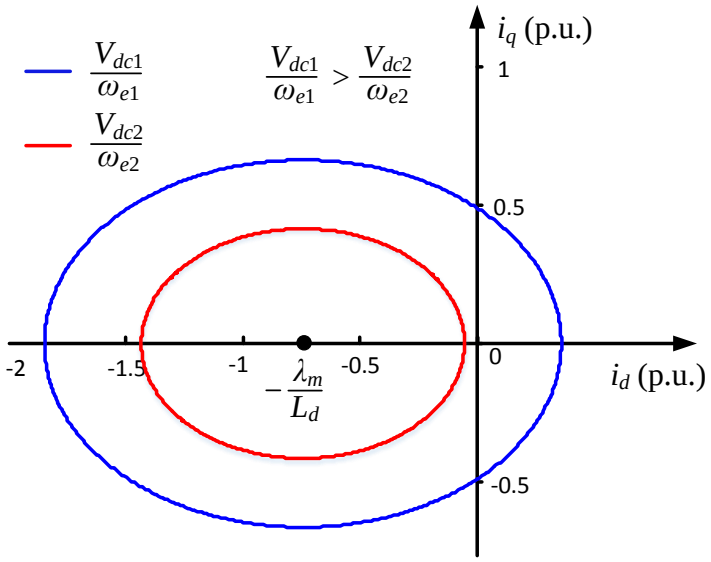

Figure 2.5. Voltage operation limits of an interior PM synchronous machine in the i_d-i_q plane

2.2.2 Field-weakening Operation

It can be seen from (2.24) and Figure 2.5 that the voltage limit becomes smaller as the ratio of DC bus voltage and machine speed decreases. Since the DC bus voltage is always limited in a drive system, the voltage limit will eventually shrink into the left side of the *q*-axis as the speed keeps increasing. Therefore, in practice, a negative *d*-axis current is often applied for a PM synchronous machine to avoid voltage saturation and increase output torque in high-speed operations. This is termed as the field-weakening operation of PM synchronous machines, because a negative *d*-axis current always produces a magnetic field that weakens the magnetic field of the permanent magnet in the air gap.

The voltage limit illustrates a possible operating area for a PM synchronous machine under a given set of machine speed and DC bus voltage. The specific

operating point (i_d, i_q) of the PM synchronous machine is realized by controlling the inverter switching signals using current vector control.

2.3 Control Algorithms of PM Synchronous Machines

In general, the electromagnetic torque of PM synchronous machines can be calculated from the stator currents in the *dq* rotating reference frame as [13], [15]:

$$T_e = \frac{3}{2}\frac{P}{2}\left(\lambda_{ds} iq - \lambda_{qs} i_d\right) = \frac{3}{2}\frac{P}{2}\left[\lambda_m i_q + \left(L_d - L_q\right) i_d i_q\right] \tag{2.25}$$

where λ_m is the flux linkage of the PM, L_d the *d*-axis inductance, L_q the *q*-axis inductance, *P* the number of poles. Therefore, the output torque can be fully controlled by the *d*-axis and *q*-axis currents. Next, several typical closed-loop control algorithms are presented.

2.3.1 Current Vector Control

The basic scheme of current vector control of PM synchronous machines is demonstrated in Figure 2.6. The phase currents are measured and fed into the controller in proportion. The controller calculates the *d*-axis and *q*-axis currents using Clarke and Park transformations based on the rotor position angle sensed by a resolver or an encoder. Due to the positive correlation between V_d and i_d, V_q and i_q (see in (2.19)), two proportional-integral (PI) regulators are used to generate the command *d*-axis and *q*-axis voltages for SVPWM generation. The rotor position angle is used to conduct the inverse Park transformation.

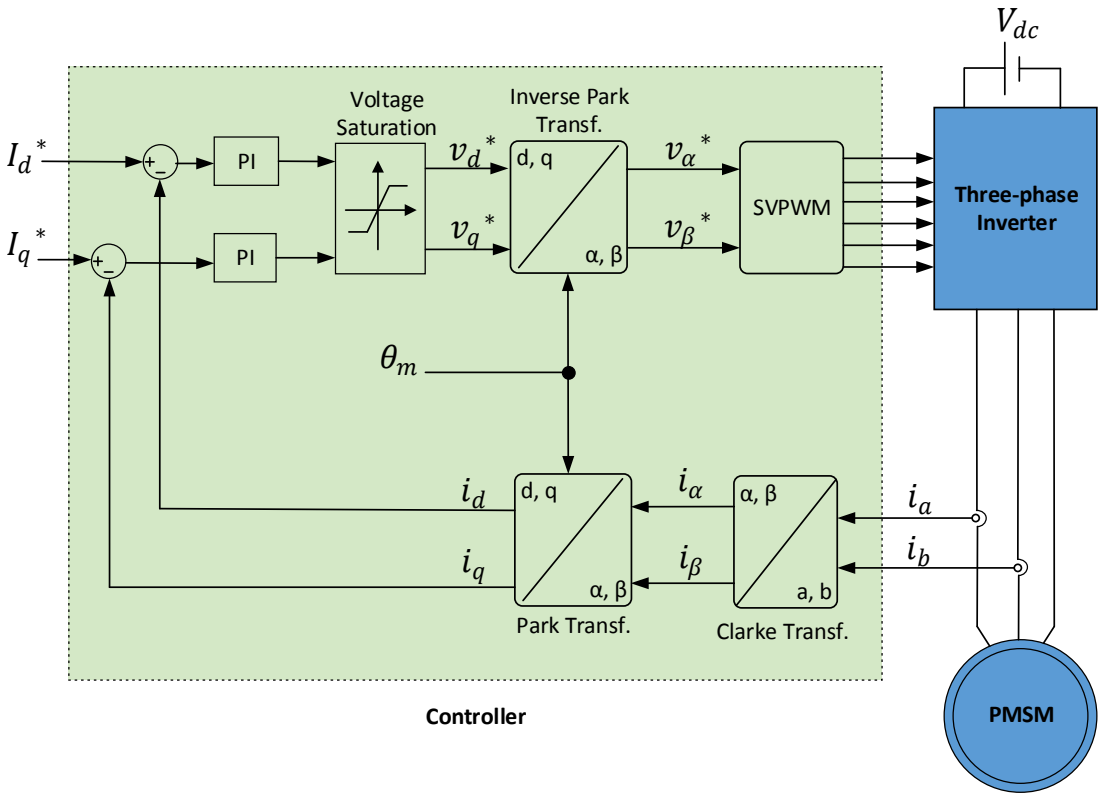

Figure 2.6. Basic scheme of current vector control for PM synchronous machines

2.3.2 **Speed Closed-loop Control**

The relation between the output torque and the speed of PM synchronous machines is given by:

$$T_e = T_l + B\omega_m + J\frac{d\omega_m}{dt} \tag{2.26}$$

where T_e is the output electromagnetic torque, T_l the load torque, B the coefficient of friction, ω_m the mechanical angular velocity of the electric machine, and J the moment of inertia. Here the machine speed is positively correlated to the output torque. Additionally, the output torque is positively correlated to the q-axis current in (2.25), where L_d is less than L_q for an interior PM synchronous machines. Therefore, a speed

closed loop can be built with a PI regulator generating the command *q*-axis current. The speed closed-loop control of PM synchronous machines is thereby built based on current vector control, as illustrated in Figure 2.7.

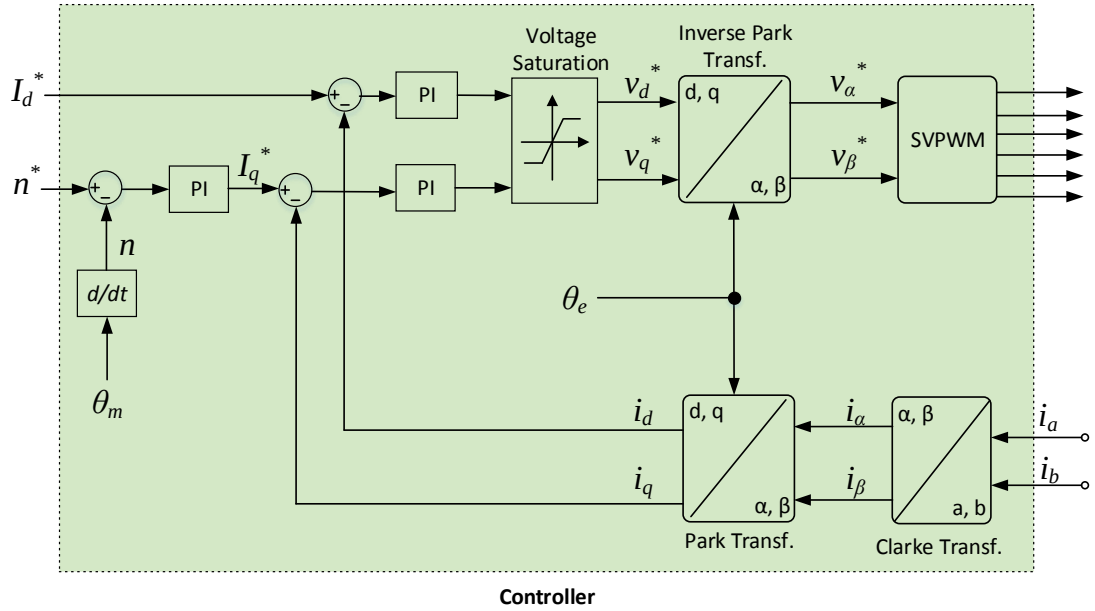

Figure 2.7. Basic scheme of speed closed-loop control for PM synchronous machines

In practice, a PI regulator is widely used to build a closed-loop control based on the positive or negative correlation between two quantities. This technique will be used again for the DC bus capacitor discharge in the next chapter.

2.3.3 **Decoupling Current Regulator**

Although it has been a standard to use current PI regulators in the *dq* rotating reference frame for current regulation of AC electric machines (see in Figure 2.6), the design of current regulators is improved by modeling and analyzing the system with complex vector notation [18], [19] and transfer-matrix approach [20]. The complex vector modeling is only applicable to machines without saliency such as surface

PMSMs and induction machines. The transfer-matrix approach can be applied to machines with or without rotor saliency.

The complex vector modeling starts with the current control of an RL load. Figure 2.8 shows the classic current PI regulator with an RL load in the synchronous reference frame, with the assumption that the controller output voltages are ideally applied to the load by the inverter ($V_d^*=V_d$ and $V_q^*=V_q$). It is impossible to obtain a single-input-single-output (SISO) transfer function between the command current and the feedback current on either axis due to the *dq* coupling in the load. However, if we map each pair of d- and *q*-axis quantities (f_d and f_q) into a complex vector in the form:

$$\boldsymbol{F}_{qd} = f_q - jf_d \tag{2.27}$$

the multiple-input-multiple-output (MIMO) system in Figure 2.8 can be merged into a SISO system as shown in Figure 2.9. This approach is termed as the complex vector modeling.

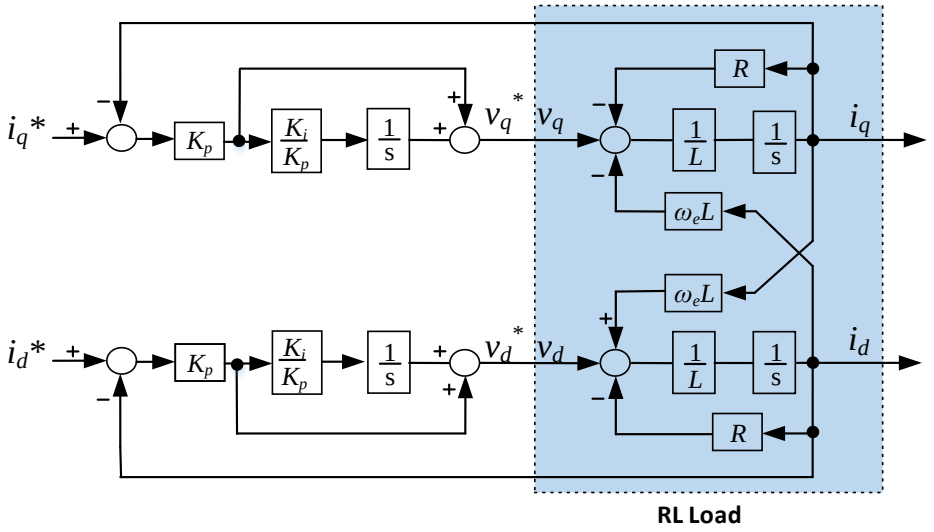

Figure 2.8. Block diagram of classic current PI regulator with RL load in synchronous reference frame

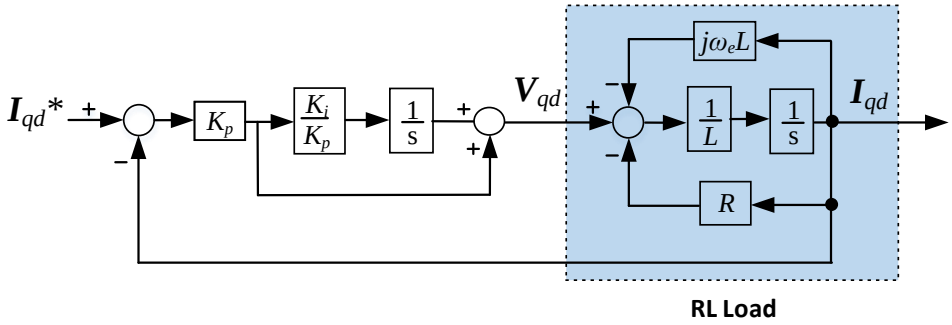

Figure 2.9. Complex vector representation of PI current regulator with RL load in synchronous reference frame

The open-loop transfer function of the SISO system using complex vector modeling is:

$$\boldsymbol{G_1(s)} = \left(K_p + \frac{K_i}{s}\right)\left(\frac{1}{sL + R + j\omega_e L}\right) = \frac{K_p(s + \frac{K_i}{K_p})}{sL(s + \frac{R}{L} + j\omega_e)} \tag{2.28}$$

In designing the current regulator, the pole-zero cancellation is often desired to improve the system dynamic performance and stability. Therefore, a decoupling form of current regulator is designed for a complete pole-zero cancellation, as shown in Figure 2.10. The open-loop transfer function becomes:

$$\boldsymbol{G_2(s)} = \left(K_p + \frac{K_i}{s} + \frac{j\omega_e K_p}{s}\right)\left(\frac{1}{sL + R + j\omega_e L}\right) = \frac{K_p(s + \frac{K_i}{K_p} + j\omega_e)}{sL(s + \frac{R}{L} + j\omega_e)} \tag{2.29}$$

where the proportional gain K_p and integral gain K_i are designed to satisfy $K_i/K_p=R/L$. Accordingly, the closed-loop transfer function is written as:

$$\boldsymbol{H(s)} = \frac{\boldsymbol{G_2(s)}}{1 + \boldsymbol{G_2(s)}} = \frac{\frac{K_p}{L}}{s + \frac{K_p}{L}} \tag{2.30}$$

The closed-loop bandwidth is thus calculated as:

$$\omega_{bw} = \frac{K_p}{L} \tag{2.31}$$

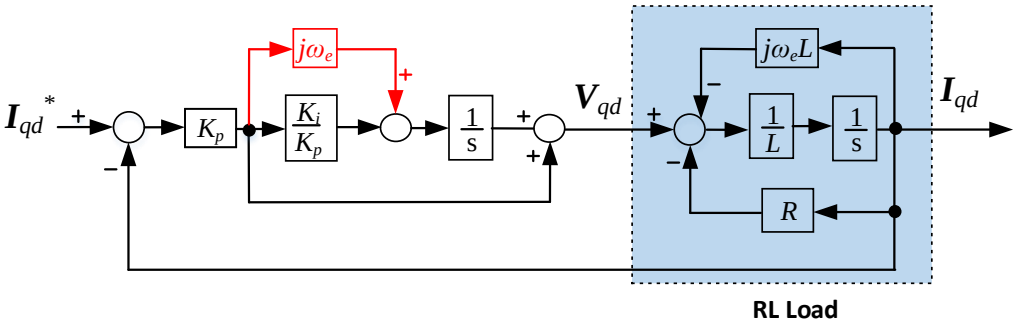

Figure 2.10. Complex vector representation of decoupling PI current regulator with RL load in synchronous reference frame

For a surface PMSM load, the decoupling current regulator is the same as an RL load but with additional decoupling of the back EMF. The decoupling current regulator for a surface PMSM is shown in Figure 2.11, where $\hat{\omega}_e$ and $\hat{\lambda}_m$ are the estimated electrical angular velocity and PM flux linkage; both the *d*-axis and *q*-axis inductances are equal to L_s; the stator winding resistance is R_s. The estimated back EMF $\hat{\omega}_e\hat{\lambda}_m$ is decoupled in the current regulator so that the surface PMSM can be modeled using complex vector. To achieve the pole-zero cancellation, the controller gains are chosen as:

$$K_p = \hat{L}_s \cdot \omega_{bw} \tag{2.32}$$

$$K_i = \hat{R}_s \cdot \omega_{bw} \tag{2.33}$$

where ω_{bw} is the desired closed-loop bandwidth; $\hat{L}_s$ and $\hat{R}_s$ are the estimated values of L_s and R_s. The improved performance of this decoupling current regulator is validated through their complex vector root loci and complex vector frequency responses [18].

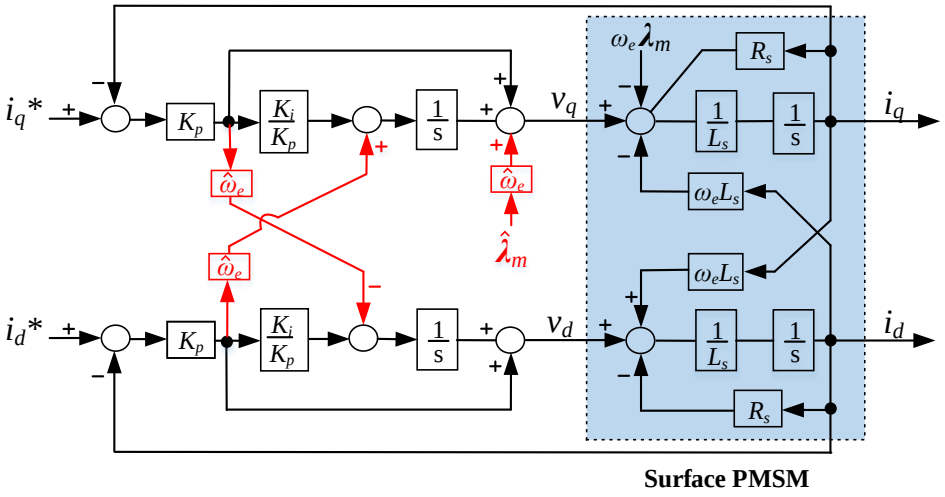

Figure 2.11. Decoupling current regulator for surface PMSM load in synchronous reference frame

For an interior PMSM load, the decoupling current regulator is designed by modeling the MIMO system with 2-dimensional matrices and solving the controller in a form of 2-D transfer matrices [20]. The decoupling current regulator for an interior PMSM is shown in Figure 2.12. Similar to the complex vector modeling, the estimated back EMF $\hat{\omega}_e\hat{\lambda}_m$ is decoupled in the current regulator, and the controller gains are chosen as:

$$K_{pd} = \hat{L}_d \cdot \omega_{bw} \tag{2.34}$$

$$K_{pq} = \hat{L}_q \cdot \omega_{bw} \tag{2.35}$$

$$K_{id} = K_{iq} = \hat{R}_s \cdot \omega_{bw} \tag{2.36}$$

where ω_{bw} is the desired closed-loop bandwidth; $\hat{L}_d$, $\hat{L}_q$ and $\hat{R}_s$ are the estimated values of the *d*-axis inductance, *q*-axis inductance and stator resistance. It should be noted that the decoupling current regulator for a PMSM using transfer-matrix modeling becomes the same as the one using complex vector modeling when L_d equals L_q.

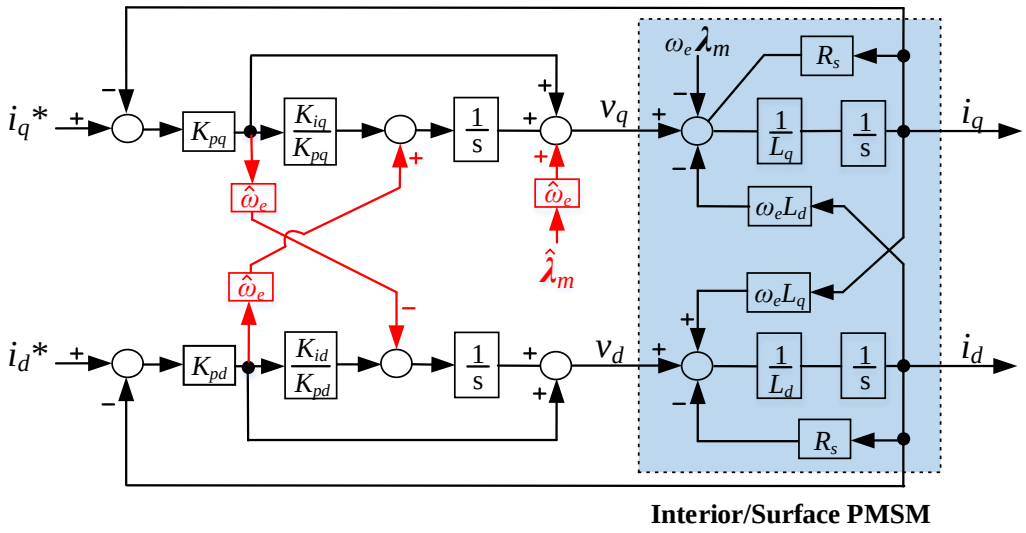

Figure 2.12. Decoupling current regulator for interior PMSM load in synchronous reference frame

The decoupling current regulator for an interior PMSM is simulated in Simulink/MATLAB, and the current response is compared with that of the classic PI regulator in Figure 2.13. The system using decoupling current regulator exhibits much shorter transient time and less overshoot than the one using classic PI current regulator. This decoupling current regulator will be used for the DC bus capacitor discharge of PMSM drive systems, where the DC bus voltage may change drastically and a great dynamic performance of the current regulator is desirable.

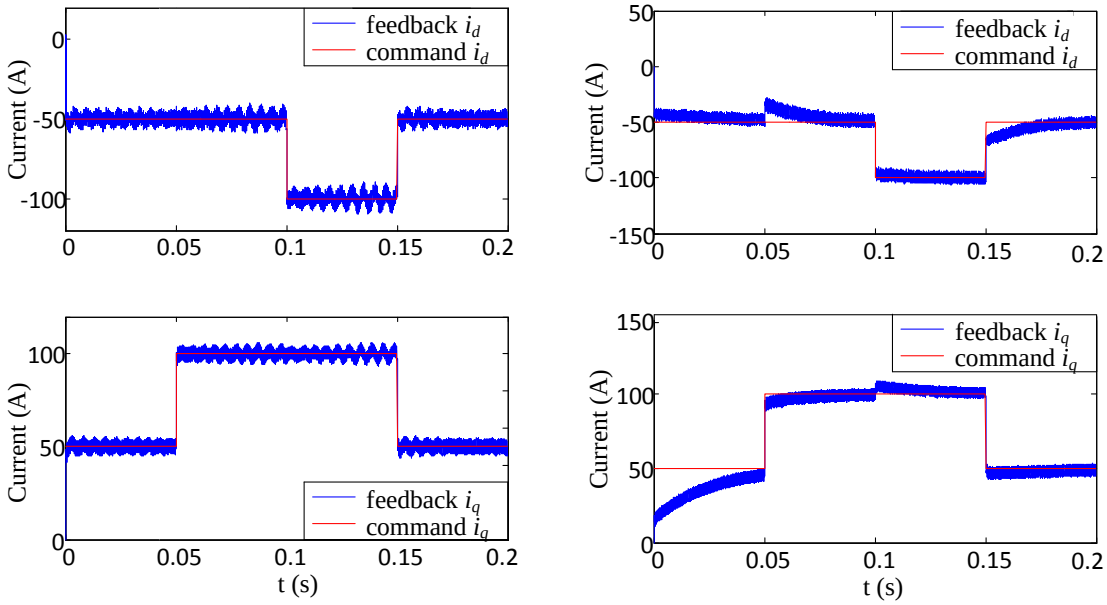

(a) decoupling current regulator (b) classic PI current regulator

Figure 2.13. Comparison of current response between decoupling current PI regulator and classic current PI regulator for interior PMSM load

3 DC Bus Capacitor Discharge of PM Synchronous Machine Drive

3.1 Control Objectives

As discussed in Chapter 1, in a key-off event of hybrid/electric vehicles, the DC bus capacitor of the electric machine drive system needs to be discharged as quickly as possible [11]. The control objective is to find a capacitor discharge path that will not cause over current or over voltage in the PM synchronous machine drive system. Because the relay has already isolated the battery from the system, the capacitor can only be discharged through the inverter and the electric machine, if no other components are added. Moreover, since the PM synchronous machine runs without any load [10], the machine inherent back EMF drops slowly, in sync with the machine speed due to the mechanical inertia. As a result, the back EMF always affects the DC bus capacitor discharge, whether the IGBTs are turned off or not.

3.2 Issues with Existing Control Algorithms

One conventional solution to this discharge problem is to add a brake chopper unit in parallel with the DC bus capacitor, as illustrated in Figure 3.1. When the IGBT in the chopper unit is turned on, the DC bus capacitor can be discharged through the resistor in the chopper unit. Notice that current will flow through the inverter diodes to charge the DC bus capacitor whenever the DC bus voltage drops below the line-to-line back EMF of the electric machine. Therefore, the resistor has to consume not only the electrical energy stored in the capacitor but also the mechanical energy left in the

electric machine. As a result, the resistor used can often be large. The additional cost and space taken by the unit are not desirable in an EV electric machine drive system.

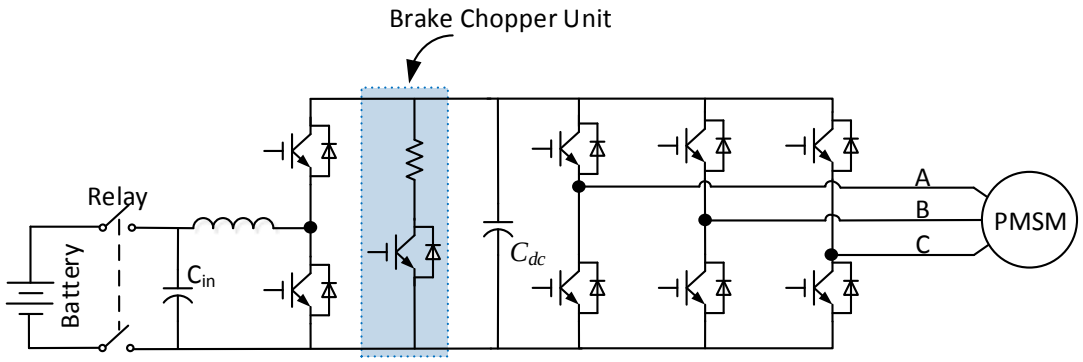

Figure 3.1. DC bus capacitor discharge through brake chopper unit

Another method used to control the capacitor discharge is to turn on all the upper IGBTs or all the bottom IGBTs of the inverter simultaneously [21], as shown in Figure 3.2. This method eliminates the current flow from the electric machine to the capacitor by shorting the electric machine stator terminals. The problem of this method is the uncontrolled short-circuit current flowing inside the electric machine, which may cause unrecoverable damage [12]. The capacitor in this situation can only be discharged through the inherent bleeder resistor (R_b). This resistor, used to dissipate the remaining charge on the DC bus capacitor in normal vehicle shutdowns, is often designed with large resistance to have very low power consumption during normal, power-on operation [22], [23]. The normal operation conflicts with a key-off event that needs the high voltage bus to quickly drop below a required level.

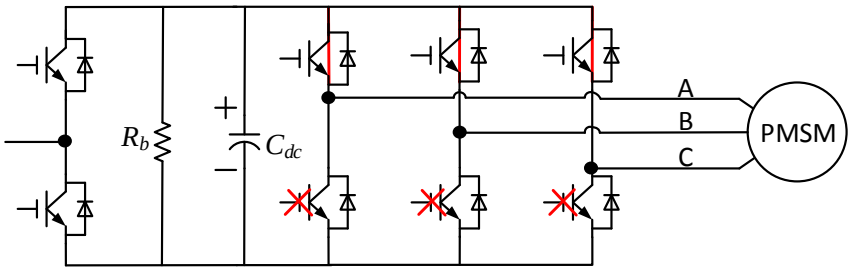

Figure 3.2. DC bus capacitor discharge with controlled short circuit of PMSM

The state-of-the-art designs manage to suppress the power flow from the electric machine to the DC bus capacitor or discharge the DC bus capacitor using the electric machine stator windings [10] [12]. However, the method proposed in [12] can only avoid a rising DC bus voltage rather than discharge the DC bus capacitor. The method proposed in [10] starts the capacitor discharge only after the machine speed drops below a certain value. Although a negative torque is generated, the time it takes to decelerate still highly depends on the mechanical inertia of the electric machine. Besides, a rising DC bus voltage is caused at the beginning, which even increases the threat of an electrical hazard. Therefore, this research will explore if a current control scheme of the PMSM can be used to first discharge the DC bus capacitor to a safe level and then wait for the electric machine deceleration. The investigation may start with analyzing the capacitor discharge power.

3.3 Proposed Control Algorithm

In order to discharge the DC bus voltage to a safe level, a large part of the energy stored in the capacitor has to be dissipated by either the inverter or the electric machine or both of them. The power flow among the DC bus capacitor, the inverter and the PM synchronous machine can be analyzed by the following equation:

$$P_{discharge} = P_{loss} - P_{gen} \tag{3.1}$$

where $P_{discharge}$ is the power of discharge of the DC bus capacitor; P_{gen} is the generation power of the electric machine; P_{loss} is the total power loss, including the inverter switching loss and conduction loss, and the electric machine copper loss, core losses and mechanical losses.

The power generated by the PM synchronous machine is directly related to its *d*-axis current i_d and *q*-axis current i_q as [15]:

$$P_{gen} = -T_e\omega_m = -\frac{3}{2}\omega_e\left[\lambda_m i_q + \left(L_d - L_q\right)i_d i_q\right] \tag{3.2}$$

where T_e is the electromagnetic torque calculated using (2.25), ω_m the mechanical angular velocity, ω_e the electrical angular velocity; the *d*-axis inductance L_d is equal to the *q*-axis inductance L_q for a surface PMSM and less than L_q for an interior PMSM. Notice that the electric machine will be decoupled from the gear mechanism and run without any load [10]. We know from (2.26) that a small positive torque can drive the electric machine to unexpected high speed and even damage the electric machine. Therefore, the *q*-axis current should be controlled either at zero or negative to ensure a zero or negative output of torque. Accordingly, the generation power (P_{gen}) becomes either zero or positive.

The quickest way to discharge the DC bus capacitor is to have the largest possible discharge power $P_{discharge}$. In other words, the power loss is maximum and the power generated by the electric machine is zero in (3.1). Since the losses in both the inverter and the electric machine are highly dependent on the current magnitude [24], [25], it is

straightforward to command a large negative i_d at the beginning of the capacitor discharge to cause a relatively large loss and avoid voltage saturation.

Notice that the capacitor cannot be directly fully discharged, because the machine speed decreases much slower than the DC bus voltage and the voltage limit ellipse shrinks drastically during discharge, which can finally cause a current regulator saturation and make the *d*-axis and *q*-axis currents unable to follow the commands. Even if all the IGBTs are turned off to avoid uncontrollable current, the inverter diodes can still be turned on by the high back EMF. Consequently, the capacitor will be recharged, with the DC bus voltage rebounding to a few hundred volts. Therefore, the speed has to drop below a certain value before the inverter can be completely shut down. In other words, the DC bus voltage should maintain at a safe voltage level before the electric machine decelerates to this certain speed.

Figure 3.3 illustrates the variation trend of the electric machine speed and DC bus voltage during capacitor discharge. The capacitor discharge can be divided into three stages:

Stage 1 (t_0~t_1): Fast discharge using zero iq and a large negative id;

Stage 2 (t_1~t_2): DC bus voltage closed-loop regulation (P_{loss}=P_{gen});

Stage 3 (t_2~end): Turn off all the inverter IGBTs.

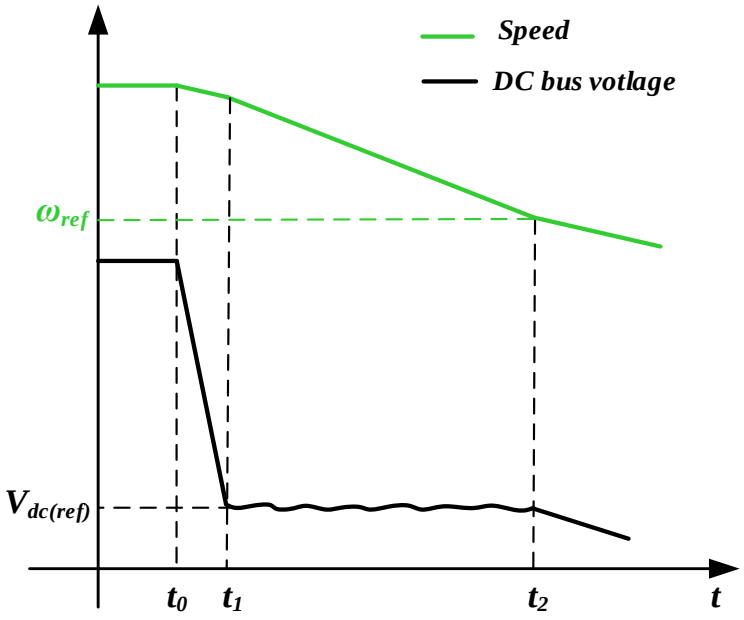

Figure 3.3. Variation trend of electric machine speed and DC bus voltage during DC bus capacitor discharge

The relay is open and the capacitor discharge starts at $t=t_0$. The DC bus voltage drops to a specific low value $V_{dc(ref)}$ at $t=t_1$, and the electric machine decelerates to the threshold mechanical speed ω_{ref} at $t=t_2$. This critical mechanical speed is related to $V_{dc(ref)}$ as:

$$\omega_{ref} = \frac{V_{dc(ref)}}{\sqrt{3}\lambda_m} \cdot \frac{2}{P} \tag{3.3}$$

where λ_m is the flux linkage of the permanent magnet, P the number of poles in the electric machine.

In order to maintain the DC bus voltage during $t=t_1 \sim t_2$, the capacitor discharge power has to be zero, namely, the loss power equal to the generation power in (3.1). This can be achieved by fixing the d-axis current and adjusting the q-axis current to

output the matching amount of generation power, or dynamically adjusting both the *d*-axis and *q*-axis currents at the same time. Next, two methods are developed for the closed-loop regulation of the DC bus voltage during discharge.

3.3.1 DC Bus Voltage Regulation Using i_q with Fixed i_d

Given that the DC bus voltage decreases for a positive discharge power ($P_{discharge}$), it can be seen in (3.1) and (3.2) that the DC bus voltage is negatively correlated to the *q*-axis current. Therefore, a DC bus voltage PI regulator is used to feed the command *q*-axis current for the current vector control, as shown in Figure 3.4. It should be noted that the proportional gain and the integral gain are both negative for the DC bus voltage PI regulator. By constructing this closed loop, the command *q*-axis current is adjusted dynamically. As a result, the *q*-axis current is adjusted in a way that makes the generation power (P_{gen}) match the loss power (P_{loss}).

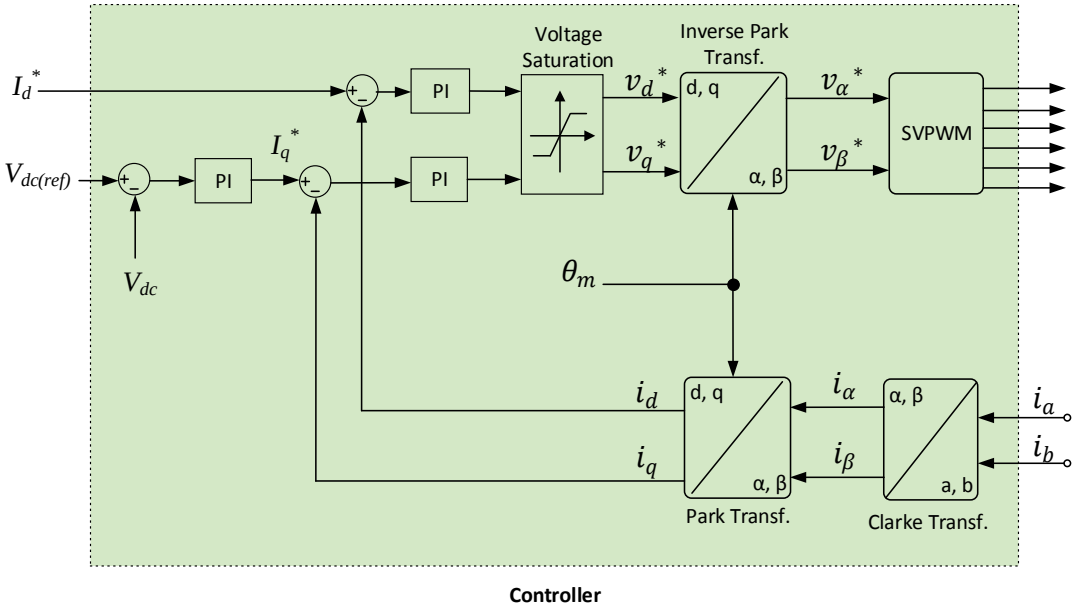

Figure 3.4. Control scheme of DC bus voltage regulation using i_q with fixed i_d

3.3.2 DC Bus Voltage Regulation Using i_q with Regulated i_d

During the fast discharge period (Stage 1), the fixed value of the *d*-axis command current (i_d^*) is often selected based on the voltage limit described in (2.24) with some margin to avoid voltage saturation, as shown in Figure 3.5. It should be noted that these voltage limits assume zero ripples on the actual (feedback) i_d and i_q in steady state. However, in practice, the actual i_d and i_q always have ripple, whose amount depends on the performance of the current regulator. Therefore, the real output command voltages of the current regulator (V_d^* and V_q^*) may still get saturated at the end of Stage 1 if the margin left is not large enough. If the same command i_d is used in Stage 2 for the DC bus voltage regulation, the voltage will remain saturated, leaving the *q*-axis current and the DC bus voltage uncontrolled.

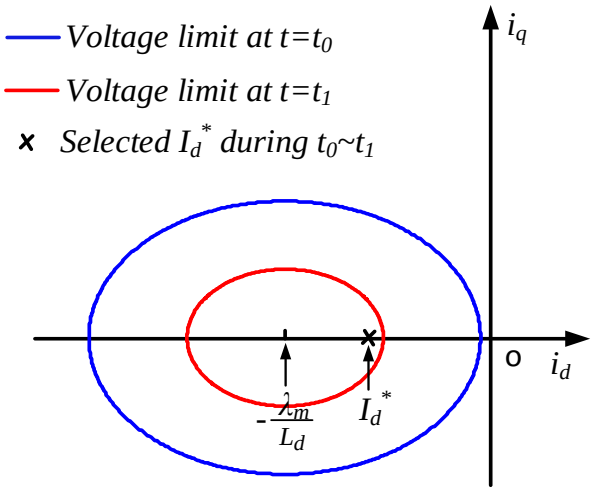

Figure 3.5. Selection of command *d*-axis current (I_d^*) for fast discharge in Stage 1.

In order to avoid the current regulator saturation in Stage 2, the *d*-axis current has to be dynamically regulated. Notice in (2.20), (2.22) and (2.24) that the PWM

modulation index, as an essential indicator of voltage saturation, is positively correlated to the *d*-axis current. Therefore, a modulation index closed loop can be constructed to generate the command *d*-axis for the current vector control, as shown in Figure 3.6. While the DC bus voltage is still regulated using *q*-axis current, the *d*-axis current is dynamically adjusted to maintain a modulation index smaller than the maximum value 1.15 (e.g. m^*=1).

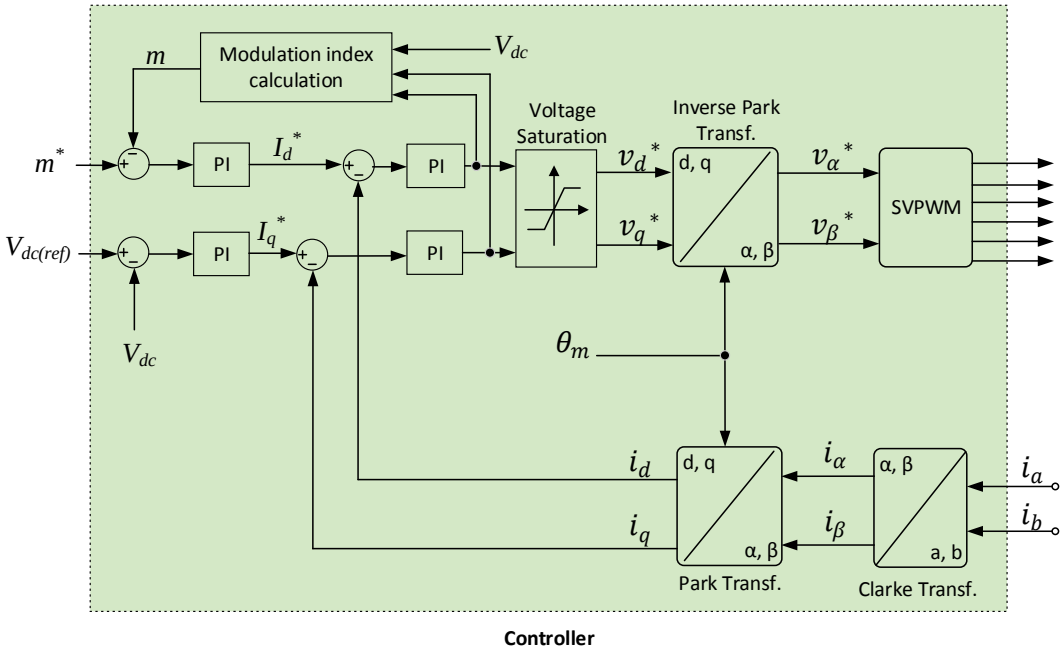

Figure 3.6. Control scheme of DC bus voltage regulation using i_q with regulated i_d

4 Computer Simulation and Experimental Verification

This chapter first introduces the modeling of the discrete-time controller with its SVPWM generation in Simulink/MATLAB. Then simulations of the DC bus capacitor discharge are conducted using both of the DC bus voltage regulation methods proposed in Chapter 3. The simulation results are presented and analyzed. The proposed control algorithms are also verified on a PMSM drive hardware platform. Both the hardware and software used for experimental verification are presented. The experimental results are discussed in detail.

4.1 Discrete-time Microcontroller Modeling

For an electric machine drive system using digital control, the controller often reads and updates the system information (current, voltage and rotor position) by sampling the analog signals from the sensors in every interrupt period. In general, the controller works in a discrete-time domain, while the models of the electric machine and inverter are continuous. Therefore, to make the closest approximation to the real system, it is necessary for all the blocks in the controller to update once every sampling period while the inverter and electric machine in each simulation step, which is much smaller compared to the sampling period.

4.1.1 Triggered Subsystem

Figure 4.1 illustrates the simplified simulation modules of a PMSM drive system in Simulink. A *Triggered Subsystem* is used to simulate the controllers shown in Figures 2.6, 2.7 and 3.6 in the discrete-time domain. The blocks in the triggered

subsystem run only when it is triggered, in this case, when the *Repeating Sequence Stair* counts to zero and a rising edge appears. The *Repeating Sequence Stair* is used to simulate an up and down count of the microcontroller, with a maximum count value of 250. Therefore, while the inverter and the electric machine are simulated as continuous-time models by running them in a simulation step of 0.4 *us*, the controller updates all the blocks inside in a period of:

$$T_c = 250 \times 2 \times 0.4\,us = 200\,us \tag{4.1}$$

which makes the sampling frequency and the switching frequency 5 kHz.

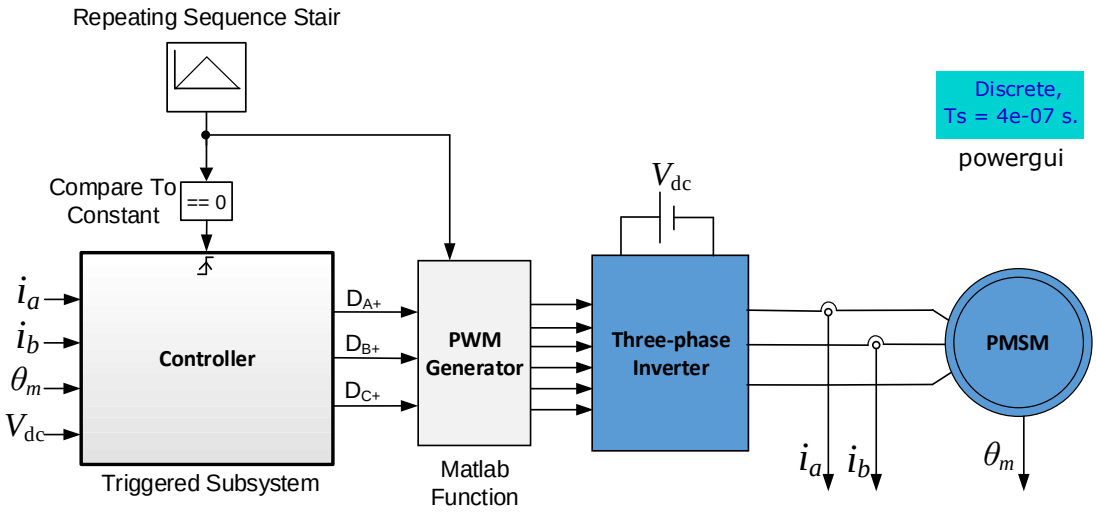

Figure 4.1. Triggered subsystem used for simulation of controller in MATLAB/Simulink

4.1.2 **Space Vector PWM Generation**

Figure 4.2 demonstrates how the duty cycles of the three upper IGBTs in the inverter are calculated in the triggered subsystem. With the command *d*-axis and *q*-axis voltages (v_d^* and v_q^*) calculated from the current PI regulators (see in Figure 2.6), the original three-phase reference voltages (v_a^*, v_b^* and v_c^*) are obtained using inverse

Park transformation and inverse Clarke transformation. In order to generate SVPWM, the zero-sequence voltage needs to be injected as [26]:

$$v_0 = -\frac{1}{2}(v_{max}^* + v_{min}^*) \tag{4.2}$$

where v_{max}^* and v_{min}^* are the maximum and minimum voltages of the three phase voltages at any given time. The duty cycle of each upper IGBT in the inverter is then calculated using the zero-sequence injected voltages as [27]:

$$D_{x+} = \frac{1}{2}\left(1 + \frac{v_x^* + v_0}{V_{dc}/2}\right), \quad x \in \{A, B, C\} \tag{4.3}$$

In practice, the duty cycle calculated in the present interrupt cycle is actually used for the PWM generation in the next cycle. Therefore, a unit delay is added at each output port of duty cycle.

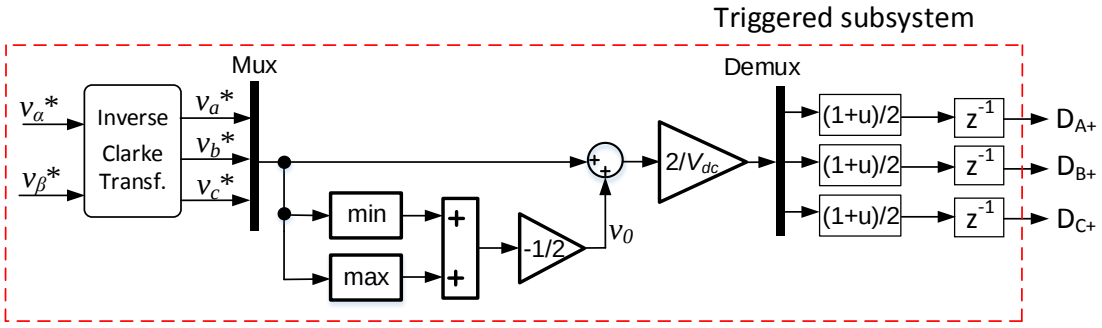

Figure 4.2. Duty cycle calculation for SVPWM in MATLAB/Simulink

After the duty cycle of each upper IGBT is calculated, the *Repeating Sequence Stair* can serve as a counter and the switching signals of all IGBTs can be generated using a MATLAB function (see in Figure 4.1). The flowchart of the MATLAB function is illustrated in Figure 4.3, where 'S_{x+}=0' represents the upper switch in Phase *x* (*x*=*A*, *B*, or *C*) is off, 'S_{x+}=1' upper switch on and "S_{x-}" for the bottom switch.

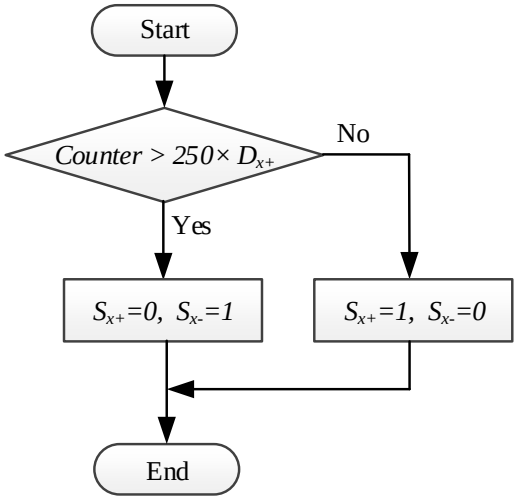

Figure 4.3. Flowchart of generating switching signals for Phase *x* using upper switch duty cycle (*x*=*A*, *B*, or *C*)

4.2 Simulation Results

Simulations are conducted in Simulink/MATLAB for only a short period to validate the feasibility of the proposed algorithm in Stage 1 and Stage 2 of the DC bus capacitor discharge. Notice that the electric machine speed is almost unchanged from the beginning of the discharge to the beginning of Stage 2 (see in Figure 3.3) due to the mechanical inertia. Therefore, as an approximation, the PMSM is set to the constant speed mode in simulations with a speed of 3000 RPM.

Recall that in Stage 2 of the capacitor discharge, the DC bus voltage can be regulated using *q*-axis current with the command i_d either fixed or regulated by the modulation index closed loop. Next, simulation results are shown for these two situations respectively.

4.2.1 DC Bus Capacitor Discharge with Fixed i_d

The DC bus capacitor is first discharged with a fixed command i_d in both Stage 1 and Stage 2 and the command iq fixed at zero in Stage 1 and regulated by the DC bus voltage closed loop in Stage 2. The initial DC bus voltage is set at 300V and the reference DC bus voltage $V_{dc(ref)}$ selected to be 70V. As shown in Figure 4.4, the relay is open at t=0.05s and the command *q*-axis current is set to zero immediately, with the feedback *q*-axis current following the command well. The DC bus voltage drops drastically after t=0.05s due to the large loss caused by the large current. When the DC bus voltage drops below the preset reference (70V), the DC bus voltage closed-loop control is activated and starts generating a negative command i_q for the current vector control, with the command i_d remaining at -200A. It can be seen that the DC bus voltage can maintain around 70V during t=0.1s~0.2s using i_q regulation. The modulation index is also observed to be smaller than 1.15 during discharge, meaning that the selected *d*-axis command current is large enough to avoid current regulator saturation. The zoom-in view of the modulation index shows that the controller updates the calculation in a period of (0.089s-0.088s)/5=0.2ms, which coincides with the switching cycle of 5 kHz. This simulation validates that the DC bus capacitor can be quickly discharged using a zero i_q and a large negative i_d, and the DC bus voltage can maintain at a certain low value by dynamically adjusting i_q using the DC bus voltage PI regulator.

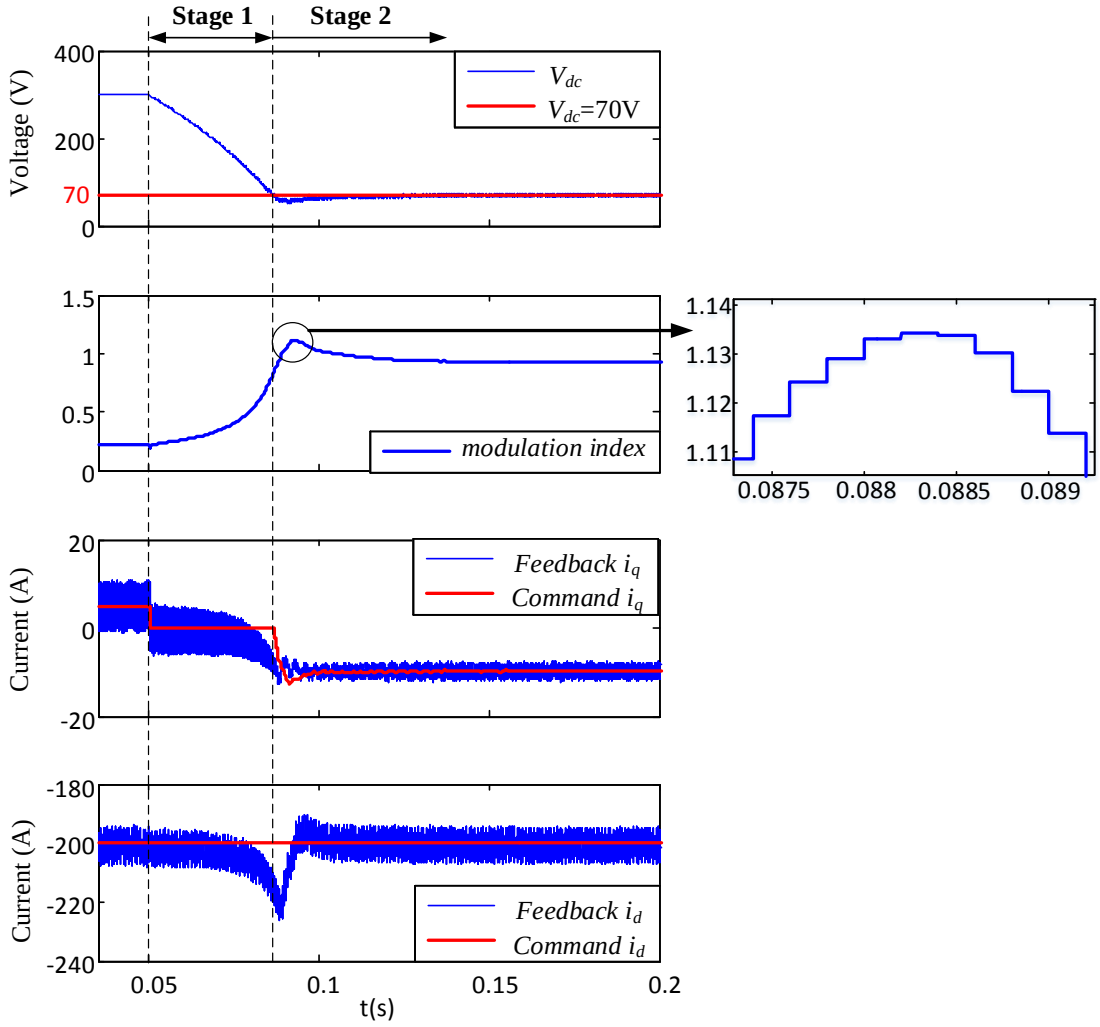

Figure 4.4. Simulation results of DC bus capacitor discharge using i_q regulation and fixed command i_d

4.2.2 DC Bus Capacitor Discharge with Regulated i_d

The DC bus capacitor is then discharged with the command i_d fixed in Stage 1 and regulated by the modulation index closed loop in Stage 2. The command i_q is fixed at zero in Stage 1 and regulated by the DC bus voltage closed loop in Stage 2. As shown in Figure 4.5, the relay is open at t=0.05s and the command *d*-axis and *q*-axis currents are set to -150A and 0A immediately for the DC bus capacitor fast discharge. When

the DC bus voltage drops to $V_{dc(ref)}$=70V, the DC bus voltage PI regulator starts to provide a negative command i_q. Meanwhile, the command i_d is adjusted by the modulation index PI regulator to have a higher magnitude (around -190A). After a short period of transient, the DC bus voltage maintains at 70V and the modulation index at 1. It should be noted that the modulation index arises to 1.4 during the transient. In other words, over-modulation (or current regulator saturation) appears during the transient. The additional command i_d regulation using the modulation index closed loop helps bring the modulation index back to 1 and avoid current regulator saturation in the steady state. This simulation validates that the additional modulation index closed loop can adjust the command i_d to have a magnitude large enough to eliminate voltage saturation in Stage 2, even if the voltage does get saturated in Stage 1.

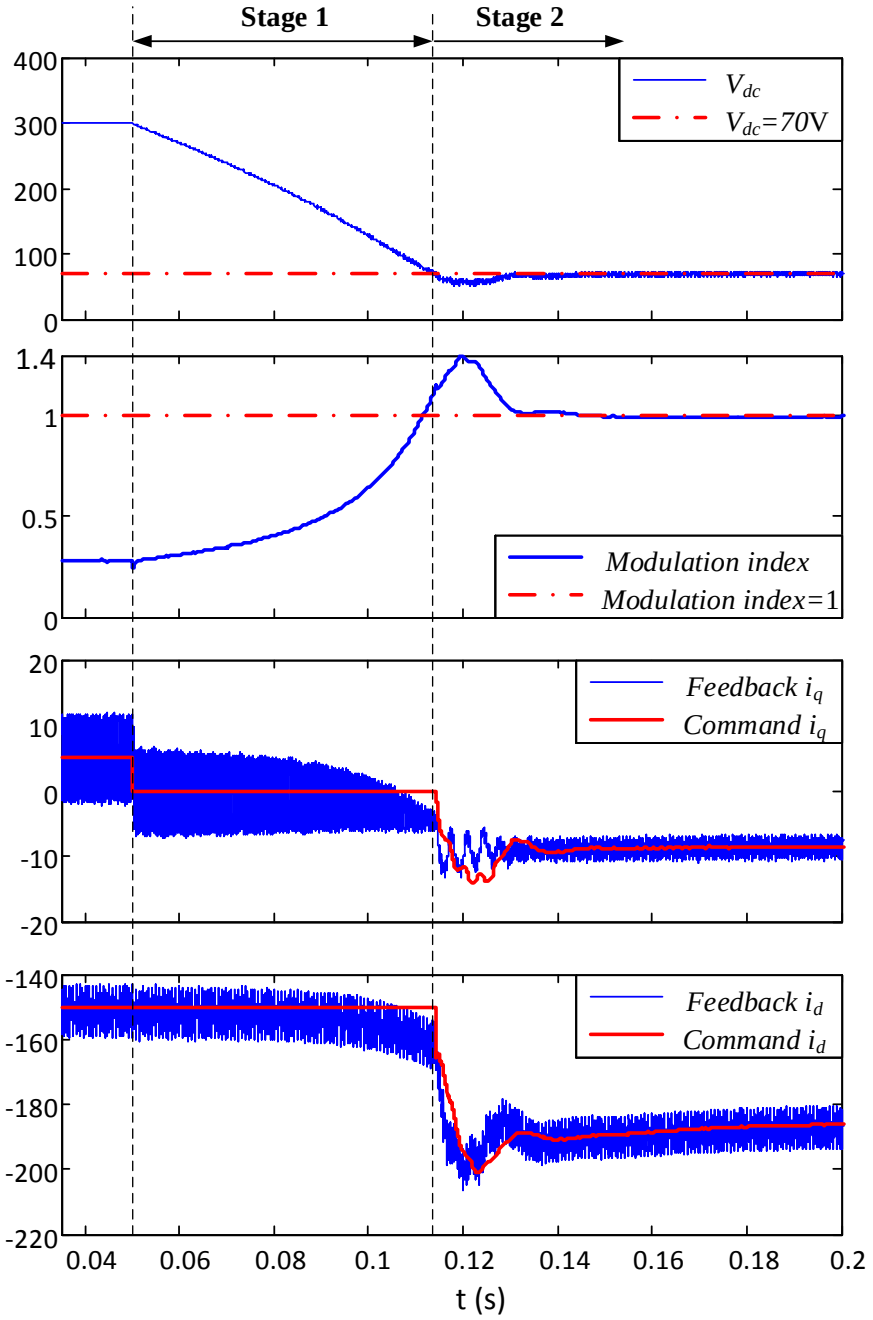

Figure 4.5. Simulation results of DC bus capacitor discharge using both *d*-axis and *q*-axis command current regulations

4.3 Hardware Integration

Figure 4.6 illustrates the block diagram of the hardware platform used for experimental verification, with the actual system shown in Figure 4.7. The system mainly consists of the interior PM synchronous machine, the voltage-source inverter, the controller and the DC power supply. Since the electric machine runs under zero load during the DC bus capacitor discharge, the dynamometer (dyno) is decoupled with the interior PMSM under test (see in Figure 4.6). A resolver to digital (R/D) board is used to convert the resolver analog output to the digital signals that the controller can use to calculate the rotor position angle. The DC bus capacitor is integrated in the voltage-source inverter. A solid state relay (SSR) is used between the DC power supply and the inverter, and the controller will apply the DC bus capacitor discharge algorithm immediately after it opens the SSR.

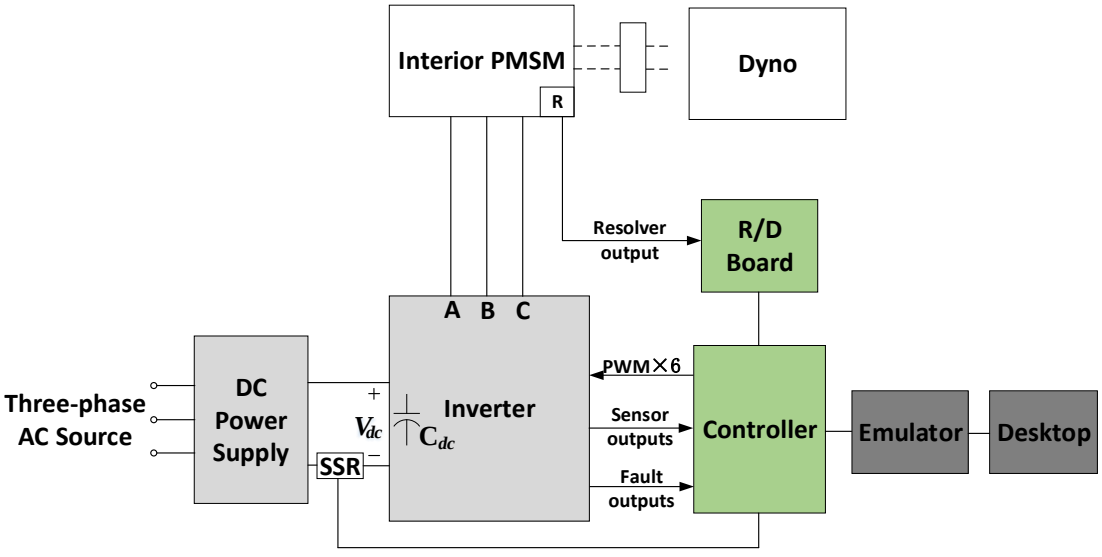

Figure 4.6. Block diagram of PM synchronous machine drive system.

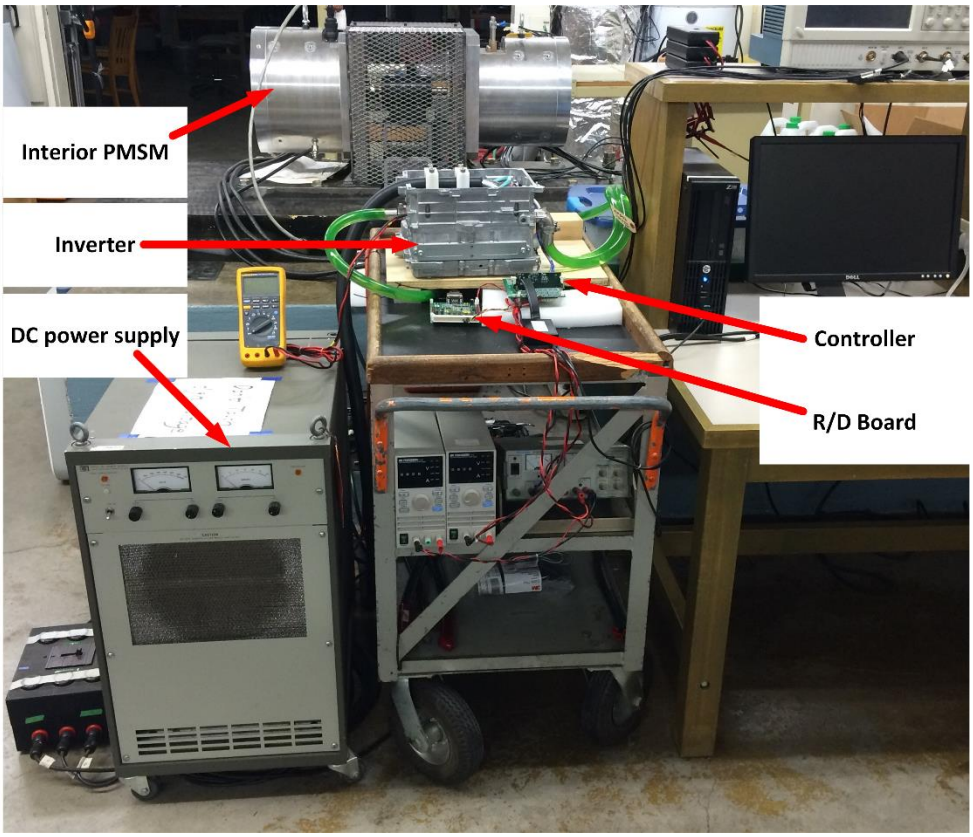

Figure 4.7. Hardware platform of PM synchronous machine drive system

4.3.1 **PM Synchronous Machine**

The electric machine under test is an interior PM synchronous machine. The parameters of this interior PMSM are listed in Table 4.1.

Table 4.1 Parameters and ratings of PMSM under test

Parameters and ratings	Values
Rated power (kW)	100
Rated phase current (A peak)	500
Number of poles	8
D-axis inductance L_d (mH)	0.16
Q-axis inductance L_q (mH)	0.26
Stator phase resistance R_s (Ω)	0.01
PM flux linkage (V s)	0.056

4.3.2 **Voltage-source Inverter**

The voltage-source inverter contains an input DC bus filter capacitor (1100 *uF*), a three-phase inverter (six pairs of IGBTs and diodes), the gate drive circuits, the current sensors for all phases, the DC bus voltage sensor, and the IGBT temperature sensors. The gate drive circuits receive PWM signals from the controller and turn on or turn off the IGBTs in the inverter. The sensors provide the controller voltages proportional to the phase current, DC bus voltage and IGBT temperature. They also send out the failure state of each phase to the controller if any over-current, over-voltage or over-temperature appears.

4.3.3 **Controller**

The controller has a TMS320F28335 controlCARD from the *Texas Instruments (TI) Experimenter's Kit* integrated with an interface board, as shown in Figure 4.8. The microcontroller on the controlCARD, working under a system clock of 150 MHz, uses three of its enhanced PWM modules to generate SVPWM for the inverter and five

analog-to-digital conversion (ADC) channels to collect the information of the three-phase current, DC bus voltage and IGBT temperature.

The interface board has three major functions. Firstly, it regulates all the output voltages of the sensors to have a range of 0~3V, which is the input range of the ADC channels of the TI microcontroller. Figure 4.9 shows the schematic of the voltage conditioning circuit for one of the phase current ADC channel. The voltage conversion can be written as:

$$V_{ADC} = \frac{R_8}{R_5}\left[\frac{R_3}{R_1} \cdot V_{IN} - \left(1 + \frac{R_3}{R_1}\right) V_{REF}\right] \tag{4.4}$$

where V_{IN} is the sensor output voltage, V_{REF} a reference voltage provided on the interface board, V_{ADC} the final input voltage for the ADC channel. The selection of V_{REF} and the resistance values depend on the ranges of the sensor output voltages.

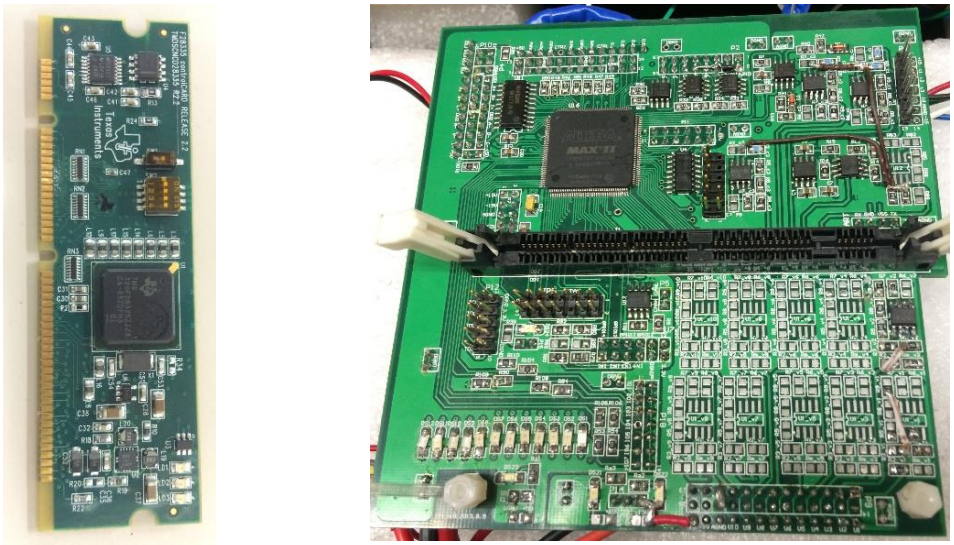

(a) F28335 controlCARD (b) interface board

Figure 4.8. Disassembled digital controller

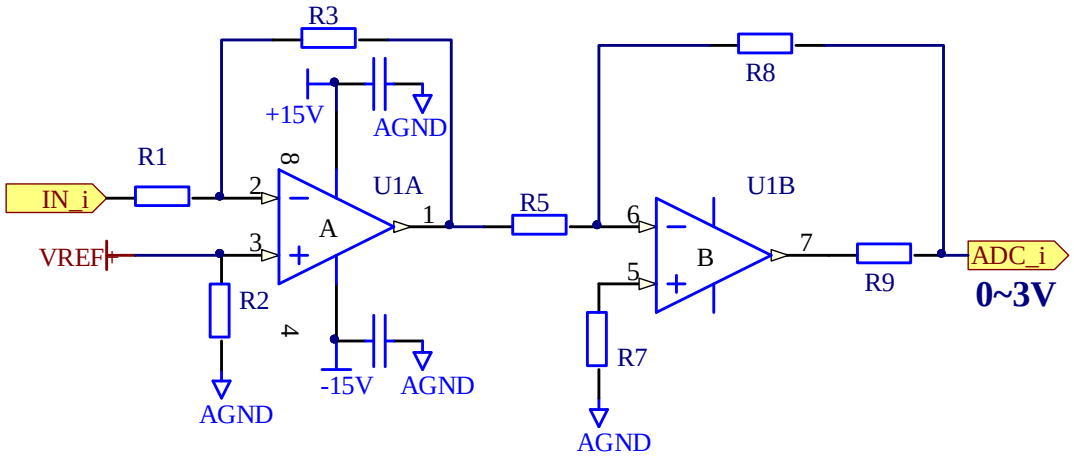

Figure 4.9. Schematic of voltage conditioning circuits for one ADC channel

The second function of the interface board is to realize the protection logic that disables all the PWM outputs to the inverter. An octal buffer chip SN74ABT541B [28] is used to convert the 0/3.3V PWM signals into 0/5V PWM signals that match the input range of the gate drive circuits in the inverter. A complex programmable logic device (CPLD) is used to AND all the failure signals (over-current, over-voltage, over-temperature) together and generate one protection signal for the disable pin of the chip SN74ABT541B. As a result, the hardware protection is triggered immediately to disable all PWM outputs no matter which failure occurs.

The third role of the interface board is to monitor the system variables and statuses. A digital-to-analog conversion (DAC) chip TLV5614CD [29] is integrated on the interface board, so that any system variable or ADC result can be converted into an analog signal and monitored on the oscilloscope. An array of light-emitting diodes (LEDs) are used to indicate the system statuses, such as whether an over-current fault occurs or not and whether the SSR is open or not.

4.4 Software Implementation

The software is compiled and downloaded into the microcontroller using TI code composer studio (CCS) v5. The controller output voltages V_d^* and V_q^* and the consequent PWM duty cycles are updated by executing the main interrupt in each switching cycle. The flow chart of the main interrupt is shown in Figure 4.10. Recall that while the stator phase currents of the PMSM are always regulated using current vector control during DC bus capacitor discharge, the *d*-axis and *q*-axis current commands are varying based on the system demand.

Figure 4.11 shows the flow chart of selecting the command current for current vector control during experimental tests. The flag bit '**sw**' is primarily set to 1 at the beginning of starting the electric machine. Since the initial rotor position is unknown, a saw-tooth shape fake rotor position angle is generated and used for the reference frame transformations. A preset pair of command currents I_{d1} and I_{q1} are used to start the electric machine and run the electric machine to a relatively low speed (around 25 RPM). After the electric machine starts, the real rotor position is obtained, and in debugging mode of CCS '**sw**' can then be changed to 2 online. Consequently, the real rotor position angle is used, and the PMSM can be accelerated to a relatively high speed using speed closed-loop control. The general purpose input/output 22 (GPIO22), used to control the relay status, remains at '1' (high level) during the acceleration. After the electric machine reaches a high speed (3150 RPM), GPIO22 is changed to '0' (low level) online to open the relay and start the DC bus capacitor discharge. In the discharge stage 2, the command i_q is fed by the DC bus voltage PI regulator and the

command i_d fed by either a large negative value (I_{d2}) or the modulation index PI regulator. In the discharge stage 3, the magnitudes of the command currents are gradually decreased to zero, and eventually all the IGBTs are disabled using GPIO24.

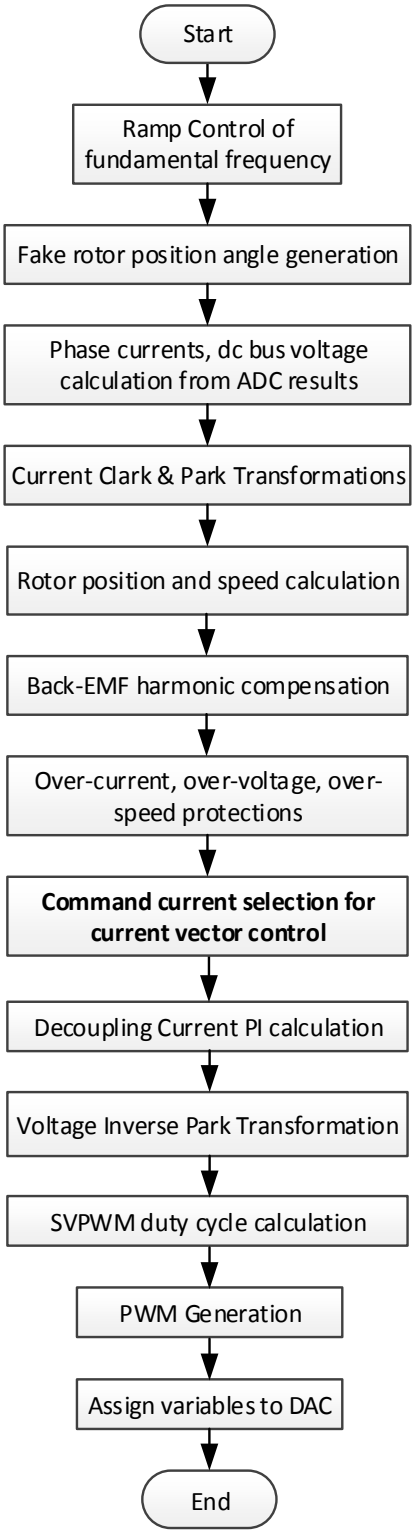

Figure 4.10. Flow chart of main interrupt

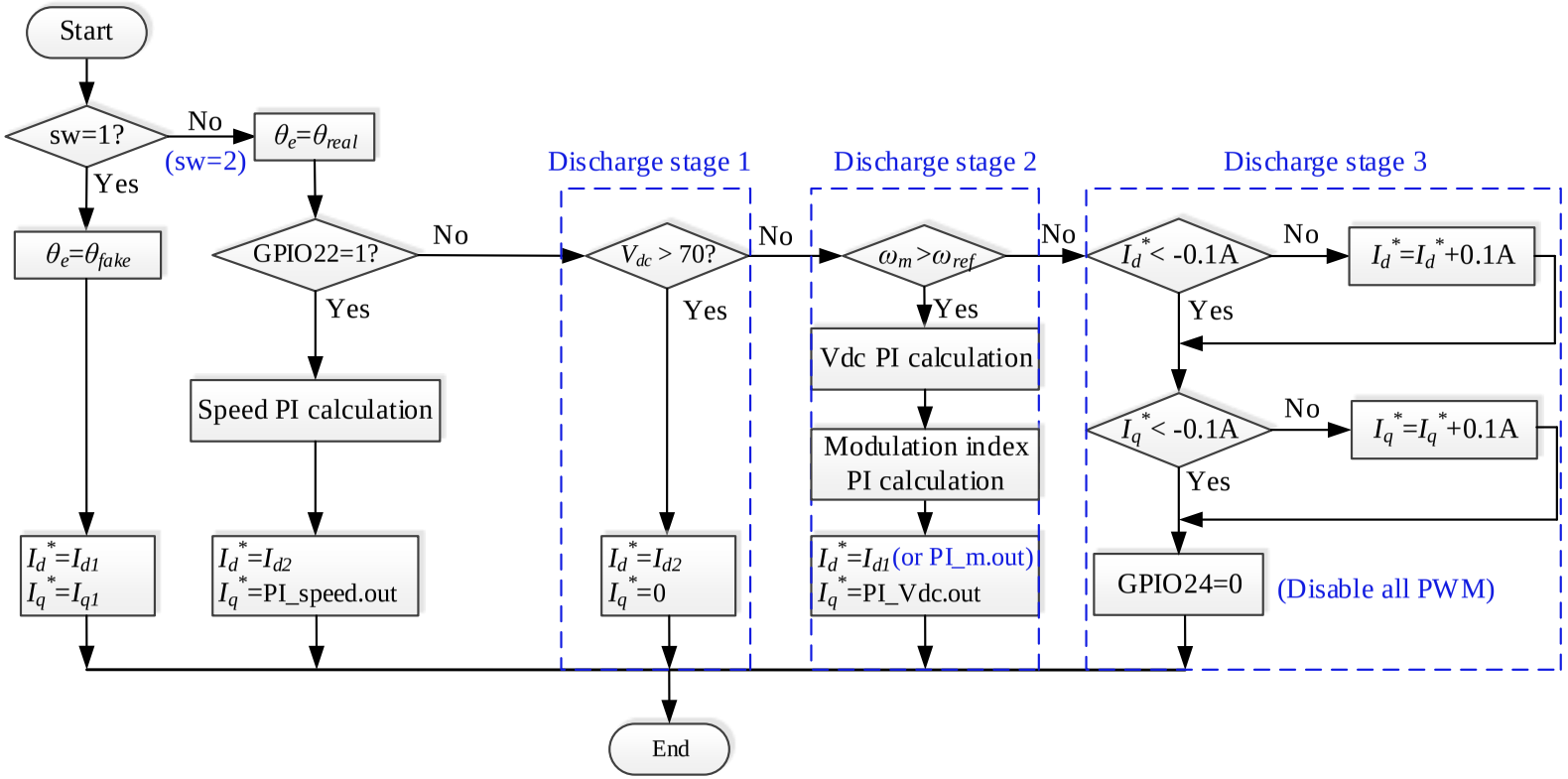

Figure 4.11. Flow chart of command current selection for current vector control

4.5 Experimental Results

In the experiments, the relay is open and the discharge starts after the PMSM reaches and maintains at 3150 RPM. The DC bus voltage prior to the discharge is 150V. The low reference voltage $V_{dc(ref)}$ is set to be 70V. In the discharge stage 2, the DC bus voltage is held at 70V using the *q*-axis current, with the command i_d either fixed or regulated by the modulation index closed loop.

4.5.1 DC Bus Capacitor Discharge with Fixed i_d

The experimental results are shown in Figures 4.12 and 4.13 for the DC bus capacitor discharge using *q*-axis command current regulation and a fixed command i_d. The command i_d is fixed at -120A in Stage 1 and Stage 2 of the discharge and gradually decreased to zero in Stage 3. While the DC bus voltage drops quickly in Stage 1 and maintains at 70V in Stage 2 as expected, it declines again at the beginning of Stage 3. This is because the small command i_q in Stage 2 is quickly decreased to zero in Stage 3 before the command i_d changes much. As a result, the generation power quickly drops to zero while the loss power remains high, resulting in the quick discharge of DC bus capacitor. After the inverter is shut down, the capacitor is recharged again due to the line-to-line back EMF and eventually drops synchronously with the machine speed.

It should be noted that the magnitude of command i_q increases during Stage 2. This can be explained by the power flow equation (3.1). Recall that the system loss power has to equal the generation power during Stage 2. While the system loss power remains almost constant due to the barely changed current magnitude, the electric

machine speed drops during Stage 2. Therefore, the electromagnetic torque has to be increased by increasing i_q so that the generation power remains constant.

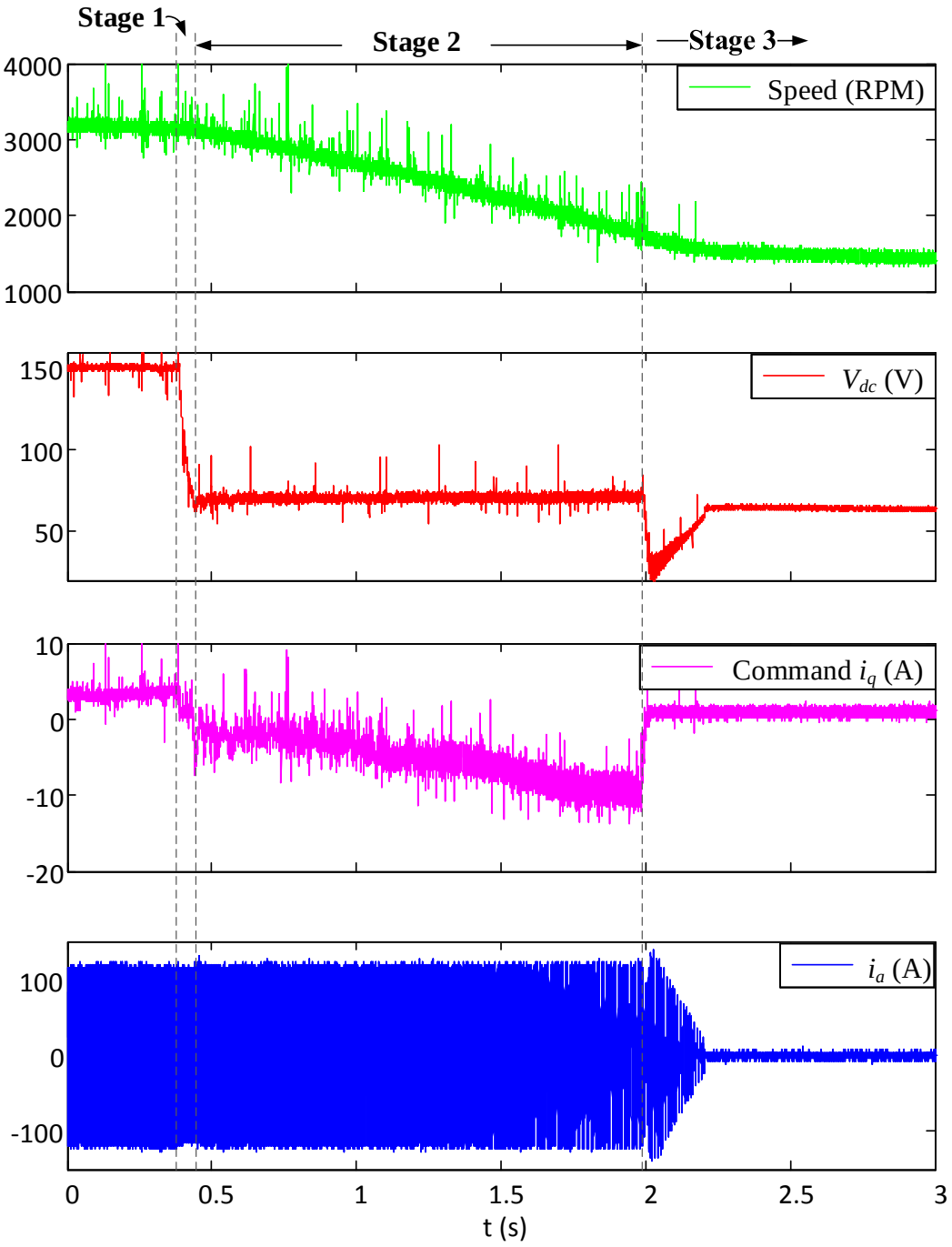

Figure 4.12. Experimental results of DC bus capacitor discharge using q-axis command current regulation and fixed i_d

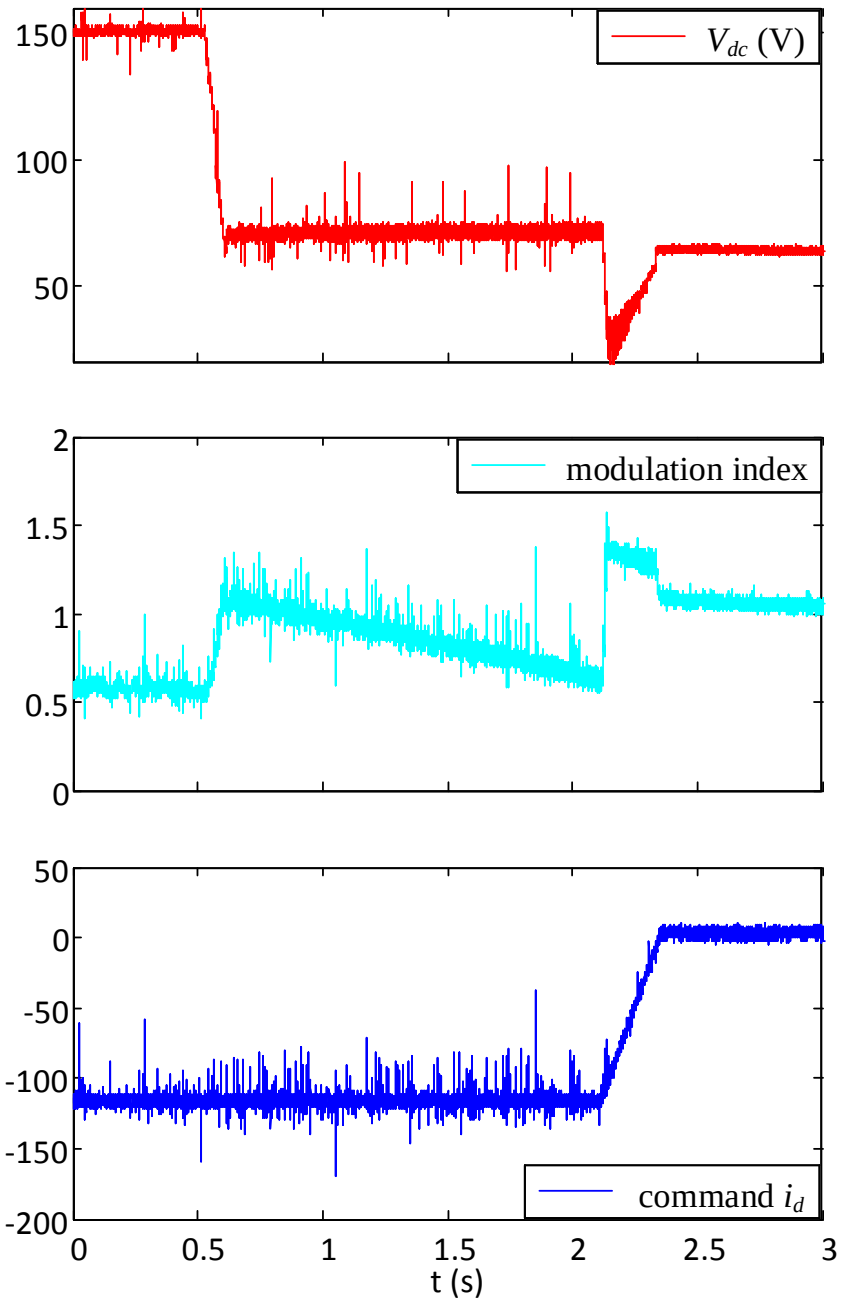

Figure 4.13. Command *d*-axis current and modulation index during DC bus capacitor discharge

4.5.2 DC Bus Capacitor Discharge with Regulated i_d

The experimental results are shown in Figures 4.14-4.16 for the DC bus capacitor discharge using both *d*-axis and *q*-axis command current regulations. The command *d*-axis current is fixed at -80A in Stage 1, regulated by the modulation index PI regulator in Stage 2, and gradually decreased to zero in Stage 3. The modulation index increases quickly in Stage 1 because the DC bus voltage drops much faster than the electric machine speed (refer to (2.20)-(2.24)). Since the fast discharge also appears at the beginning of Stage 3, the modulation index increases again there. Notice that although over-modulation appears at the end of Stage 1 (see in Figure 4.16), the modulation index is modified back and kept around 1 in Stage 2 by dynamically adjusting the command i_d. The change of command i_d in Stage 2 results in a decreasing current magnitude and thus a decreasing loss power, which indicates a decreasing generation power. Since the electric machine speed is already decreasing in Stage 2, the electromagnetic torque (or the command i_q) actually does not change much, as shown in Figure 4.15.

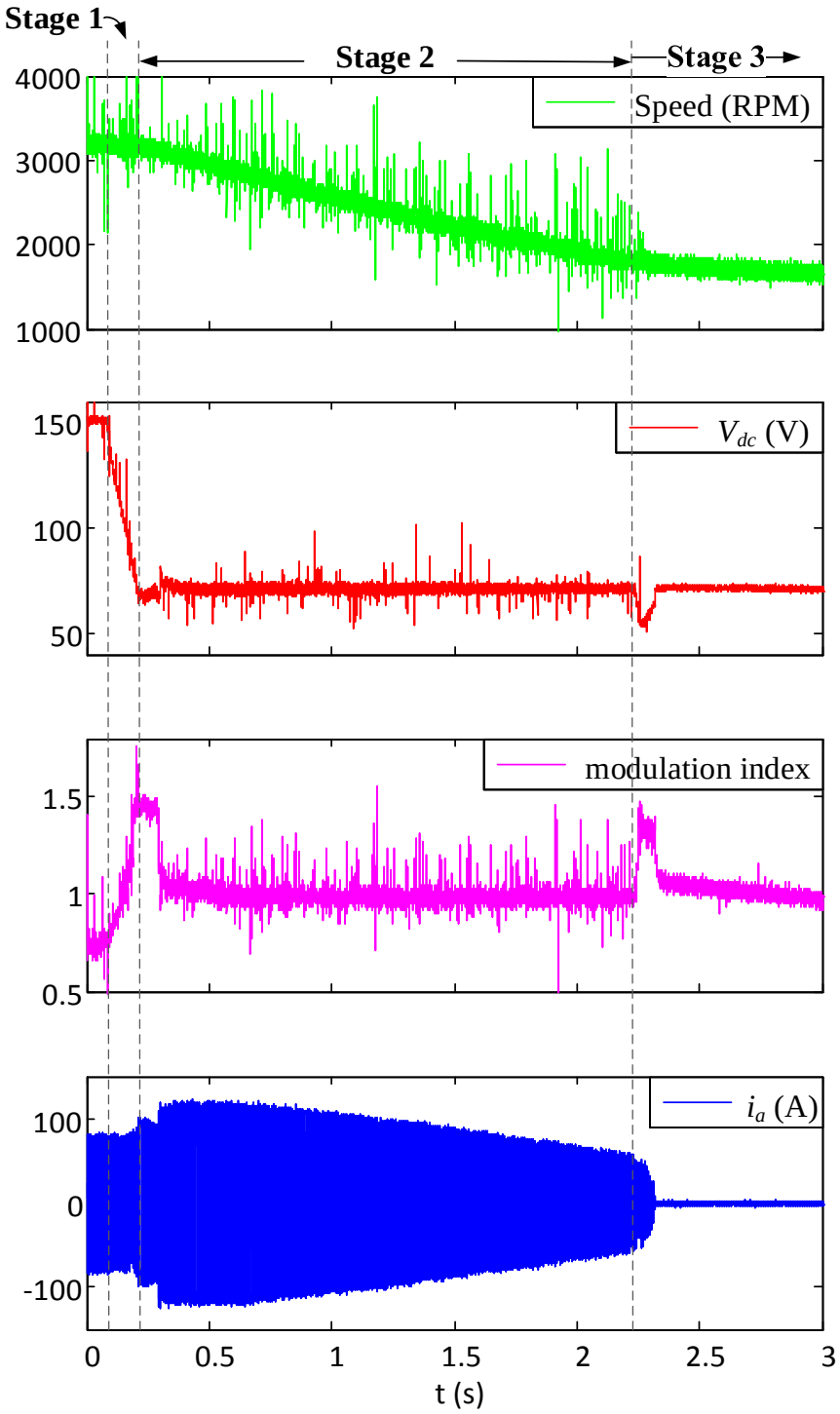

Figure 4.14. Experimental results of DC bus capacitor discharge using both *d*-axis and *q*-axis command current regulations

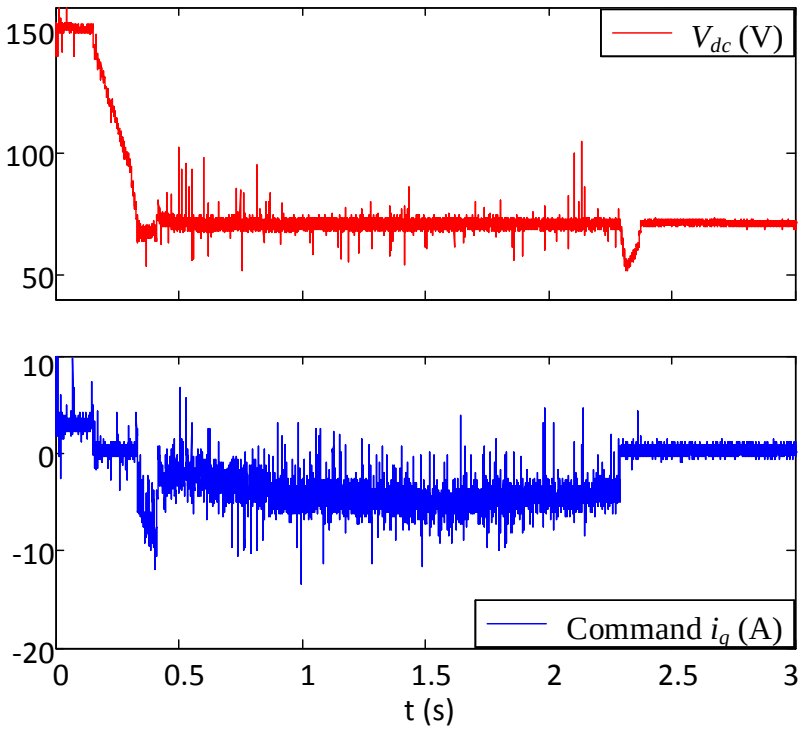

Figure 4.15. Q-axis command current regulation using DC bus voltage closed loop

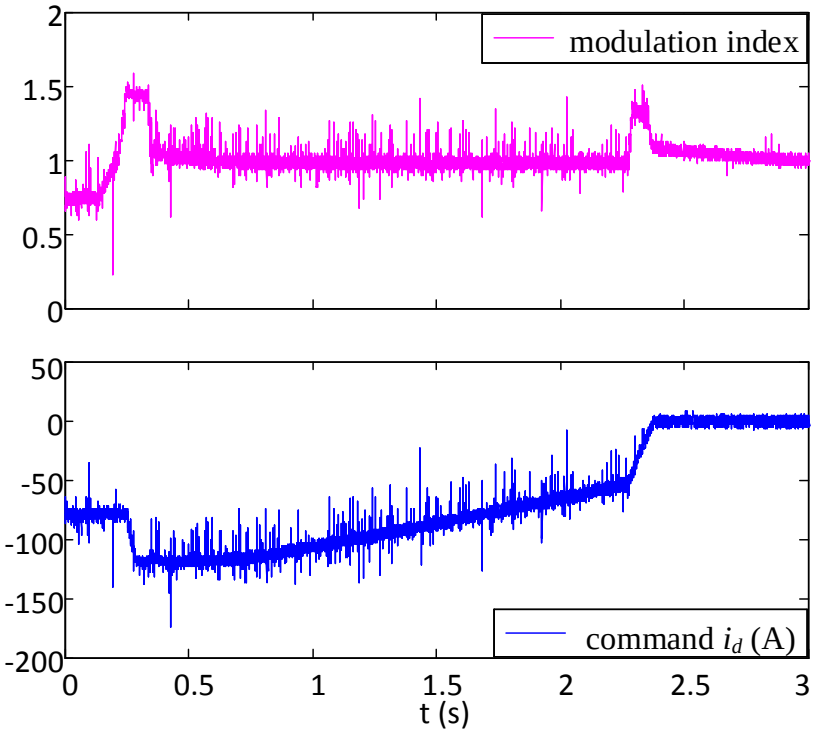

Figure 4.16. D-axis command current regulation using modulation index closed loop

5 Back EMF Harmonic Compensation

The electric machine used in this research work was designed to provide as much DC torque as possible. The back EMF of the machine contains many harmonic components. In this chapter, after analyzing the main back EMF harmonic components, a back EMF harmonic compensation algorithm is proposed. This method is verified in simulation by first building a PMSM model with harmonic components in the back EMF and then applying the proposed harmonic compensation algorithm to this PMSM with non-sinusoidal back EMF in Simulink/MATLAB. Finally, experimental results of this back EMF harmonic compensation algorithm are presented.

5.1 Back EMF Harmonic Compensation

In the analysis of a PM synchronous machine, the phase back EMF caused by the PM flux linkage is often assumed to be pure sinusoidal:

$$e_{a1} = -\omega_e \lambda_m \sin(\theta_e) \tag{5.1}$$

$$e_{b1} = -\omega_e \lambda_m \sin(\theta_e - \frac{2\pi}{3}) \tag{5.2}$$

$$e_{c1} = -\omega_e \lambda_m \sin(\theta_e + \frac{2\pi}{3}) \tag{5.3}$$

where ω_e is the electrical angular velocity, λ_m the flux linkage of the PM, θ_e the electrical angle by which the axis of the PM leads the A-axis. θ_e can be easily obtained from the rotor position angle θ_m. In practice, however, the electric machine design often makes the distribution of flux density non-sinusoidal in the air gap. As a result, the phase back EMF caused by the PM flux linkage often carries various harmonic

components. For the interior PMSM used for this research, the open-circuit line-to-line voltages are measured when it is driven by another electric machine under certain speeds as shown in Figure 5.1. The back EMF of Phase A winding is then calculated using the following equation:

$$e_a = \frac{e_{ac} - e_{ba}}{3} \tag{5.4}$$

where e_{ac} and e_{ba} are the line-to-line back EMFs. Figure 5.2 shows the Phase A back EMF measured under two different machine speeds. The spectrum analysis of the back EMF data shows that the 1st, 5th and 7th are the major harmonic components of the Phase A back EMF. While the fundamental component is given by (5.1), the 5th and 7th harmonics are accordingly calculated as:

$$e_{a5} = 0.0613\omega_e\lambda_m \cdot \sin(5\theta_e) \tag{5.5}$$

$$e_{a7} = 0.029\omega_e\lambda_m \cdot \sin(7\theta_e) \tag{5.6}$$

The flux linkage of the PM, λ_m, is estimated from the fundamental component of the phase back EMF using the following equation:

$$\lambda_m = \frac{e_{a1(max)}}{\omega_e} \tag{5.7}$$

where $e_{a1(max)}$ is the maximum value of the fundamental Phase A back EMF.

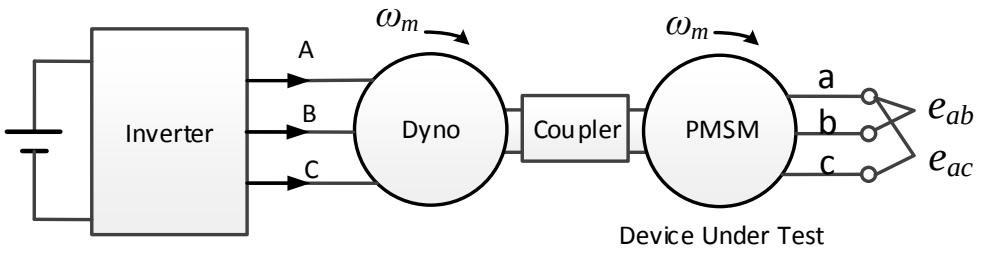

Figure 5.1. System setup for measuring back EMF caused by permanent magnets

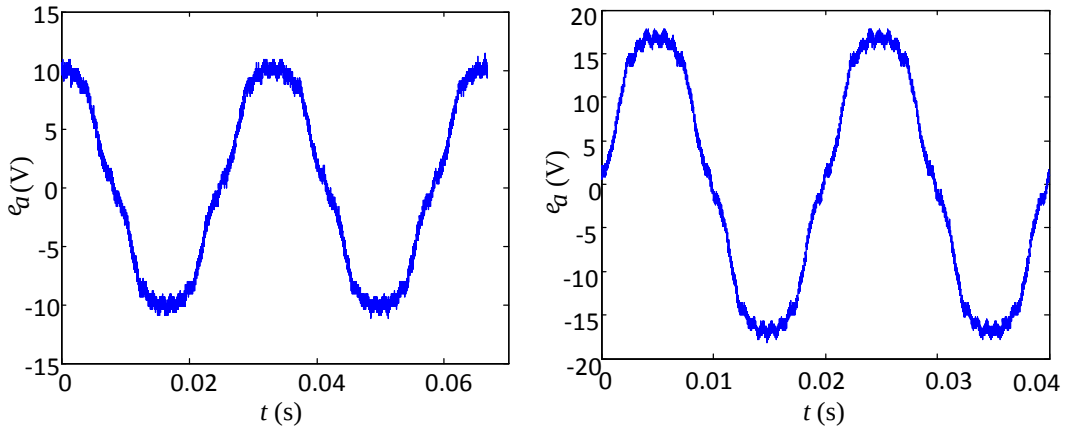

(a) n=450 RPM (b) n=750 RPM

Figure 5.2. Phase A back EMF measured under two different machine speeds

The 5th and 7th harmonics in the back EMF can result in the 5th and 7th harmonics in the current. These harmonic components cannot easily be regulated due to the limited bandwidth of the current PI regulator. Therefore, in this research, a back EMF harmonic compensation algorithm is used to compensate the effect of the back EMF harmonics on the phase currents [30]. The scheme of this harmonic compensation algorithm is shown in Figure 5.3. The 5th and 7th harmonic components of the back EMFs for Phases A and B are reconstructed using the line-to-line back EMF data demonstrated in Figure 5.2:

$$E_{ha} = 0.0613\omega_e\lambda_m \sin(5\theta_e) + 0.029 \sin(7\theta_e) \tag{5.8}$$

$$E_{hb} = 0.0613\omega_e\lambda_m \sin[5(\theta_e - 120^o)] + 0.029 \sin[7(\theta_e - 120^o)] \tag{5.9}$$

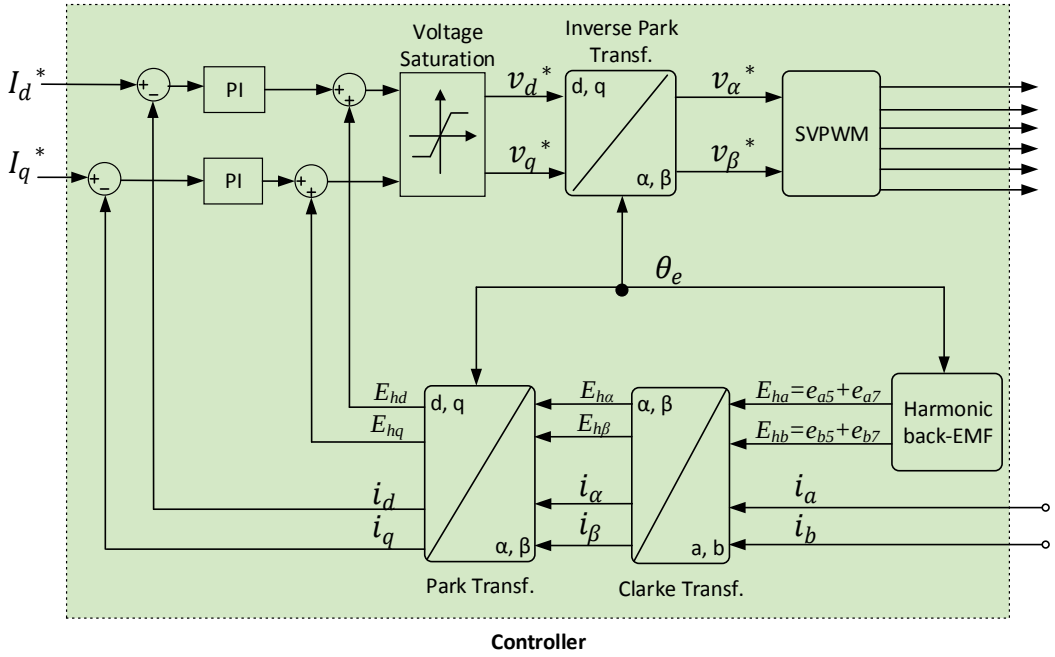

Figure 5.3. Basic scheme of back EMF harmonic compensation based on current vector control of PM synchronous machines

By injecting the harmonic back EMFs into the command voltages for SVPWM generation, the phase voltages supplied to the PMSM carry the same amount of voltage harmonics that neutralize the inherent back EMF harmonics. Next, a PMSM model with harmonic back EMF will be built in order to apply this algorithm in simulation.

5.2 PMSM Modeling with Harmonic Back EMF

Since the built-in PM synchronous machine model in the Simulink library assumes a pure sinusoidal back EMF, it is more appropriate to build a new PM synchronous machine model that can take into account the harmonic components in the back EMF.

5.2.1 **PMSM Modeling in Simulink**

Figure 5.4 shows a PM synchronous machine model built based on the existing blocks in the Simulink library. The model consists of two parts, the power flow part and the signal flow part. In the power flow part, the three phase power terminals of the electric machine (Ports A, B and C) are often connected to a power inverter or individual power switches. Thus, a virtual three-phase resistance load has to be constructed for the successful power flow between the inverter and this electric machine. In the signal flow part, all the real-time information of the electric machine is calculated based on the measured line-to-line voltages and the existing electrical equations of a PMSM. The calculated phase currents ia, ib and ic are then used to command the *Controlled Current Sources* in the power flow, so that the real phase currents flowing into the electric machine follow the calculated values. The currents flowing through the load resistors can be neglected.

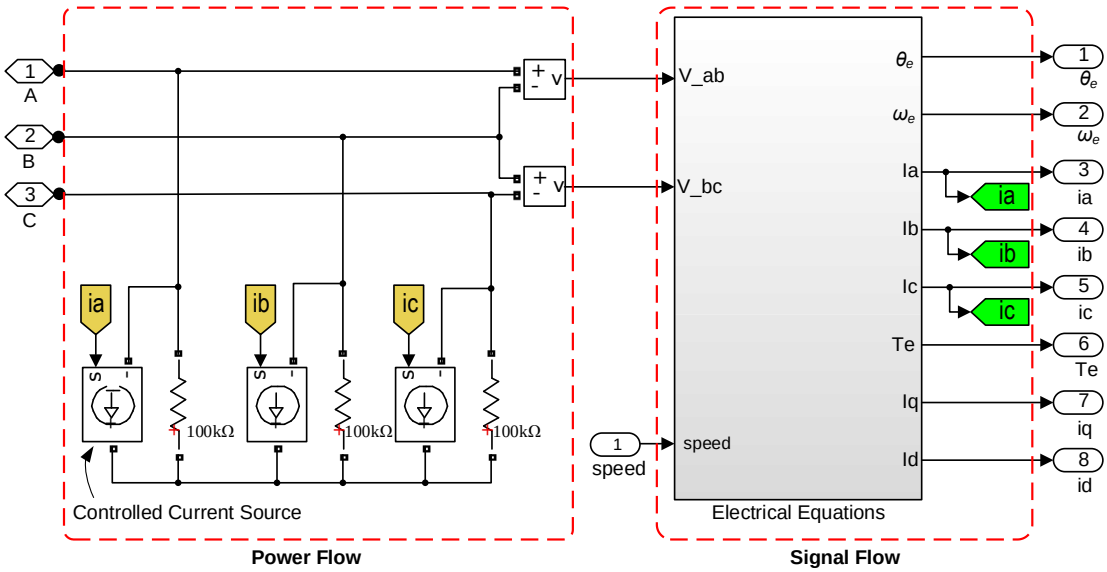

Figure 5.4. Modeling of PMSM that takes into account back EMF harmonics

5.2.2 PMSM Modeling with Back EMF Harmonics

Inside Subsystem "Electrical Equations" in Figure 5.4, the current of a PM synchronous machine is calculated with the harmonic components of back EMF taken into account, as shown in Figure 5.5. The non-sinusoidal back EMF of each phase is reconstructed using the following equations:

$$e_a = \omega_e \lambda_m \{-\sin(\theta_e) + k_1 \sin(5\theta_e) + k_2 \sin(7\theta_e)\} \tag{5.10}$$

$$e_b = \omega_e \lambda_m \left\{-\sin\left(\theta_e - \frac{2\pi}{3}\right) + k_1 \sin\left[5\left(\theta_e - \frac{2\pi}{3}\right)\right] + k_2 \sin\left[7\left(\theta_e - \frac{2\pi}{3}\right)\right]\right\} \tag{5.11}$$

$$e_c = \omega_e \lambda_m \left\{-\sin\left(\theta_e + \frac{2\pi}{3}\right) + k_1 \sin\left[5\left(\theta_e + \frac{2\pi}{3}\right)\right] + k_2 \sin\left[7\left(\theta_e + \frac{2\pi}{3}\right)\right]\right\} \tag{5.12}$$

where k_1=0.0613, k_2=0.029; λ_m is estimated using (5.7). The voltage equation used for current calculation in the *dq* rotating reference frame changes into:

$$\begin{bmatrix} V_d \\ V_q \end{bmatrix} = \begin{bmatrix} R_s & -\omega_e L_q \\ \omega_e L_d & R_s \end{bmatrix} \begin{bmatrix} i_d \\ i_q \end{bmatrix} + \begin{bmatrix} L_d & 0 \\ 0 & L_q \end{bmatrix} p \begin{bmatrix} i_d \\ i_q \end{bmatrix} + \begin{bmatrix} e_d \\ e_q \end{bmatrix} \tag{5.13}$$

where p is the derivative operator, d/dt. Notice in (2.19), for a PMSM with pure sinusoidal back EMFs, e_d and e_q are equal to 0 and $\omega_e \lambda_m$, respectively. Here for a PMSM with non-sinusoidal back EMFs, e_d and e_q are transformed from the reconstructed phase back EMFs.

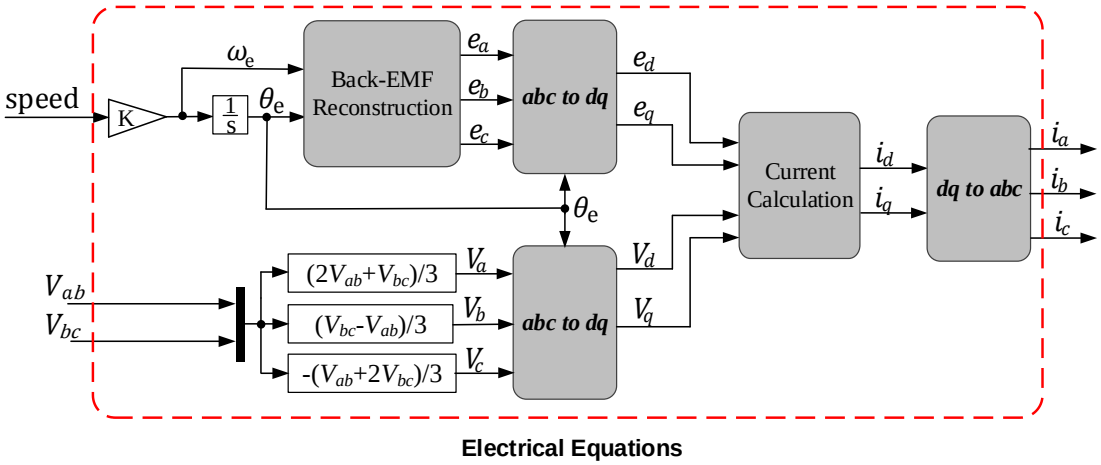

Figure 5.5. Block diagram of current calculation of PMSM with harmonic back EMF

5.3 Simulation Results

The PMSM model with harmonic components of back EMF taken into account is then simulated in Simulink/MATLAB using current vector control with a command i_d of -20A and a command i_q of 5A. The results before and after adding the proposed back EMF harmonic compensation are compared in Figure 5.6. It can be seen that the 7^{th} harmonic component of phase current is reduced after adding the back EMF harmonic compensation.

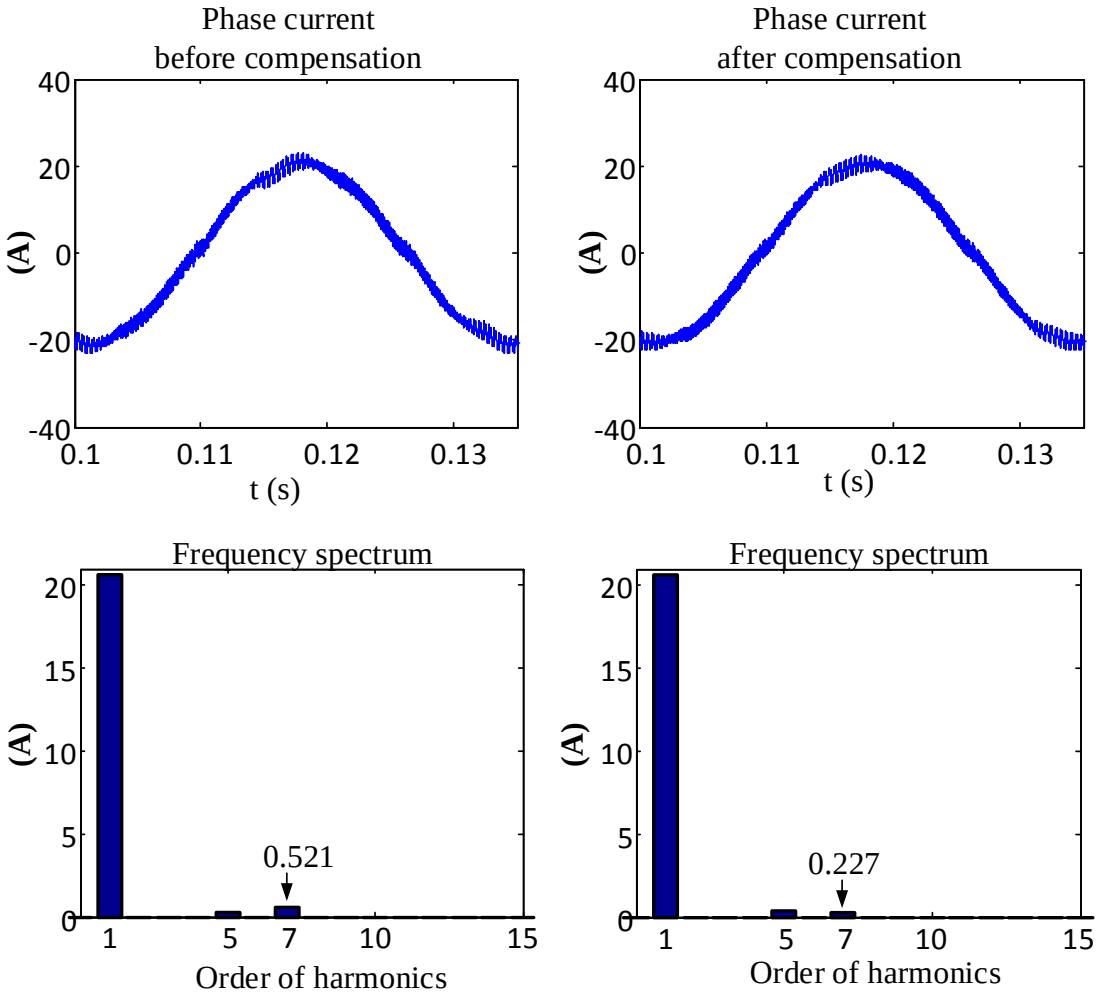

Figure 5.6. Phase current before and after back EMF harmonic compensation in simulations

5.4 Experimental Results

Experiments are conducted for the PMSM under test using speed closed-loop control with a command i_d of -20A and a command speed of 450 RPM. The results before and after implementing the proposed back EMF harmonic compensation are compared in Figure 5.7. It can be seen that the 5^{th} and 7^{th} current harmonic components are largely reduced after implementing the back EMF harmonic compensation.

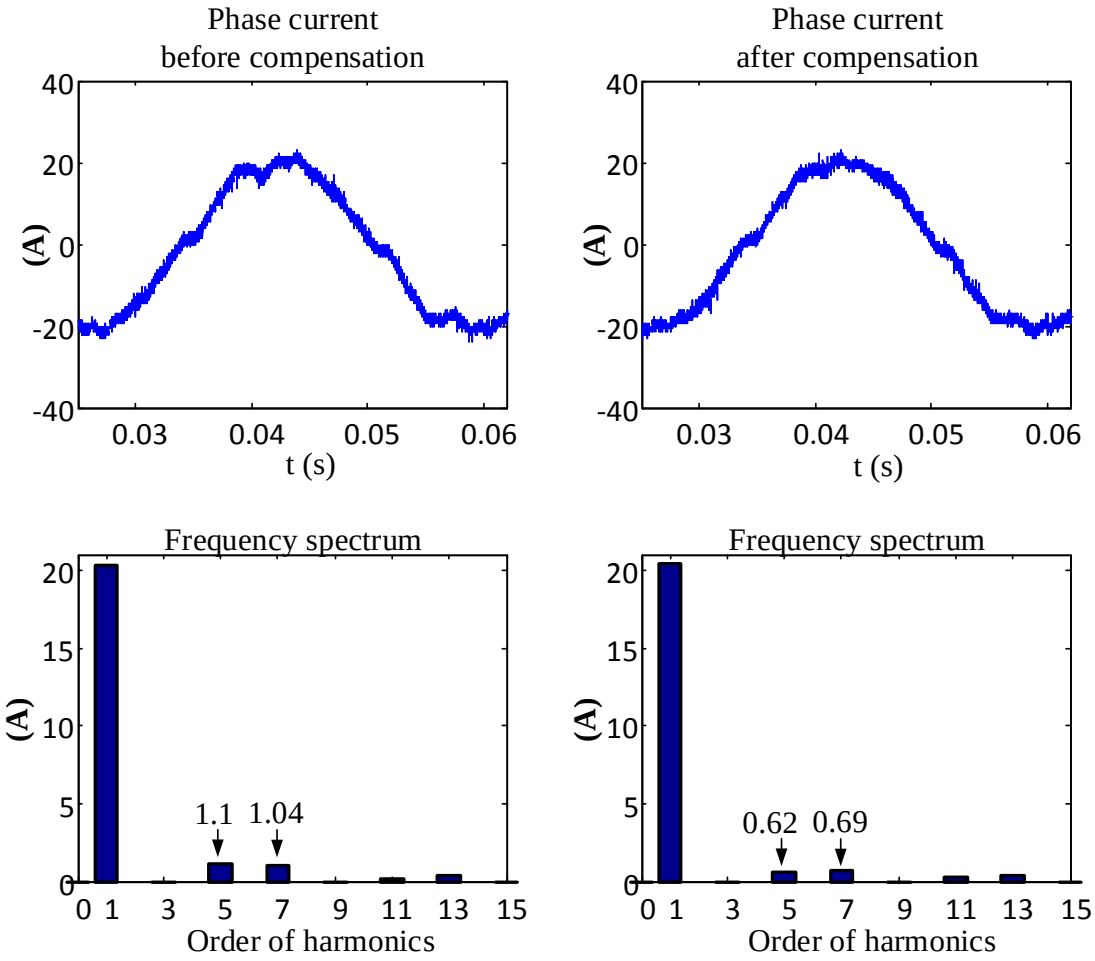

Figure 5.7. Phase current before and after back EMF harmonic compensation in experiments

6 Conclusions

This research investigates the DC bus capacitor discharge of permanent magnet synchronous machine (PMSM) drive systems for hybrid/electric vehicles upon a key-off event that needs the high voltage bus to quickly drop below a required level. By analyzing the mathematical model of PMSMs in the *dq* rotating reference frame and the system power flow during discharge, the capacitor discharge power has been found to be directly related to the *d*-axis and *q*-axis stator currents of the PMSM. Then a three-stage discharge algorithm has been developed, including the fast discharge stage, the DC bus voltage closed-loop regulation stage, and the inverter shutdown stage, to quickly and safely discharge the DC bus capacitor by dynamically adjusting the command currents for current vector control of PMSMs during these three stages.

During the DC bus voltage closed-loop regulation stage, two methods are proposed to maintain the DC bus voltage at a specific low value. The first method generates the command *q*-axis current with a DC bus voltage PI regulator while the *d*-axis command current is fixed at a large negative value. The second method, beyond the DC bus voltage closed-loop control, adds an extra modulation index closed-loop control to eliminate over-modulation by dynamically adjusting the *d*-axis current command, and thus has improved reliability.

The proposed discharge algorithm has been implemented in both simulations and experiments. In the experiments, the DC bus capacitor was discharged to have the DC bus voltage drop from 150V to 70V in less than 0.2 seconds, and the inverter was shut

down in less than 2.5 seconds. The performance of this discharge algorithm in experiments has indicated its feasibility in actual vehicle control.

The decoupling current regulator of improved dynamic response has been investigated and then implemented in both simulations and experiments to ensure that the actual stator currents of the PMSM can follow the command currents shortly in current vector control. A back EMF harmonic compensation algorithm has also been proposed and implemented in experiments to cancel the effect of the inherent back EMF harmonics of the PMSM under test.

6.1 Future work

Although the results of this research have validated the proposed method, plenty of work can still be extended. It would be more realistic to conduct the DC bus capacitor discharge under a higher level of current, voltage and electric machine speed. The actual DC bus voltage used in PMSM drive systems for hybrid/electric vehicles can be as high as 650 V, with the machine speed up to around 15000 RPM, and current magnitude as high as 500 A.

In addition, the stator phase current of the PMSM under test was found to carry relatively large 5^{th} and 7^{th} harmonic components that cannot be eliminated by the current regulator. Although the same harmonic components in the back EMF caused by the PM have, in some part, explained this phenomenon, it is still unclear why the current harmonics remain high after the back EMF harmonic compensation. More work is needed to verify if the spatial harmonics of the stator windings have been the major cause of the current harmonics.

7 Bibliography

[1] "Visualizing Electric Vehicle Sales," U.S. Department of Energy, Article, July 2013. [Online]. Available: http://energy.gov/articles/visualizing-electric-vehicle-sales

[2] "Government incentives for plug-in electric vehicles", Wikipedia. [Online]. Available: http://en.wikipedia.org/wiki/Government_incentives_for_plug-in_electric_vehicles

[3] "State & Federal Incentives, United States Incentives Map", Plug In America. [Online]. Available: http://www.pluginamerica.org/incentives

[4] C. C. Chan, A. Bouscayrol and K. Chen, "Electric, hybrid, and fuel-cell vehicles: architectures and modeling," *IEEE Transactions on Vehicular Technology*, vol. 59, no. 2, pp. 589-598, Feb. 2010.

[5] C. C. Chan, "The state of the art of electric, hybrid, and fuel cell vehicles," *Proceedings of the IEEE*, vol. 95, no. 4, pp. 704–718, Apr. 2007.

[6] MIRAI Toyota FCV. [Online]. Available: http://www.toyota.com/fuelcell/

[7] "Clean transport, Urban transport," European Commission, Transport, Sep. 2012. [Online]. Available: http://ec.europa.eu/transport/themes/urban/vehicles/road/electric_en.htm

[8] Kaushik Rajashekara, "Present status and future trends in electric vehicle propulsion technologies," *IEEE Journal of Emerging and Selected Topics in Power Electronics*, vol. 1, no. 1, pp. 3-10, Mar. 2013.

[9] "Vehicle Technologies Office: Electrical Machines," U.S. Department of Energy. [Online]. Available: http://energy.gov/eere/vehicles/vehicle-technologies-office-electrical-machines

[10] S. Ashida, K. Yamada, M. Nakamura, T. Shimana and T. Soma, "Electric vehicle, and control apparatus and control method for electric vehicle," U.S. Patent, US 8631894 B2, Jan. 2014.

[11] Y. Zhang and M. W. Degner, "Vehicle electric machine control strategy," U.S. Patent, US20140077737 A1, Mar. 2014.

[12] J. Itoh, W. Aoki, G. T. Chiang and A. Toba, "Suppression method of rising DC voltage for the halt sequence of an inverter in the motor regeneration," *IEEE Energy Conversion Congress and Exposition*, pp. 188-195, Denver, CO, USA, Sep. 2013.

[13] D. W. Novotny and T. A. Lipo, *Vector Control and Dynamics of AC Drives*. Oxford, U.K.: Clarendon, 1996.

[14] W. V. Lyon, "Transient conditions in electric machinery," *Transactions of the American Institute of Electrical Engineers*, vol. 42, pp. 157-179, 1923.

[15] Y. Zhang, "Sensorless vector control and field weakening operation of permanent magnet synchronous machines," Ph.D. dissertation, Department of Electrical & Computer Engineering, The Ohio State University, 2010.

[16] H. W. van der Broeck, H. C. Skudelny and G. V. Stanke, "Analysis and realization of a pulsewidth modulator based on voltage space vectors," *IEEE Transactions on Industry Applications*, vol. 24, no.1, pp. 142-150, Jan./Feb. 1988.

[17] J. A. Houldsworth and D. A. Grant, "The use of harmonic distortion to increase the output voltage of a three-phase PWM inverter," *IEEE Transactions on Industry Applications*, vol. IA-20, no. 5, pp. 1224-1228, Sep./Oct. 1984.

[18] F. Briz, M. W. Degner and R. D. Lorenz, "Analysis and design of current regulators using complex vectors," *IEEE Transactions on Industry Applications*, vol. 36, no. 3, pp. 817-825, May/Jun. 2000.

[19] H. Kim, M. W. Degner, J. M. Guerrero, F. Briz and R. D. Lorenz, "Discrete-Time current regulator design for AC machine drives," *IEEE Transactions on Industry Applications*, vol. 46, no. 4, pp. 1425-1435, Jul./Aug. 2010.

[20] Y. S. Jeong and S. K. Sul, "Analysis and design of a decoupling current controller for AC machines," in *Conf. Rec. IEEE IAS Annual Meeting*, pp. 2066–2073, New Orleans, LA, USA, Sep. 2007.

[21] S. Cheng, D. Wang and J. Chen, "Current measurement gain tuning for interior permanent magnet synchronous motor (IPMSM) drives using controlled short circuit tests," *IEEE Transportation Electrification Asia-Pacific*, pp. 1-6, Beijing, China, Sep. 2014.

[22] "Bleeder resistor", Wikipedia. [Online]. Available: http://en.wikipedia.org/wiki/Bleeder_resistor#Design_considerations

[23] “Resistors for high voltage applications”, TT Electronics Application Note, pp. 2. [Online]. Available: http://www.digikey.com/Web%20Export/Supplier%20Content/tt-electronics-welwyn-985/pdf/welwyn-an-resistors-for-hi-voltage.pdf?redirected=1

[24] J. O. Estima and A. J. Marques Cardoso, “Efficiency analysis of drive train topologies applied to electric/hybrid vehicles,” *IEEE Transactions on Vehicular technology*, vol. 61, no. 3, pp. 1021-1031, Mar. 2012.

[25] M. G. Thompson, C. J. Hoff and J. E. Gover, “A model to estimate effect of dc bus voltage on drive efficiency,” *IEEE Vehicle Power and Propulsion Conference*, Lille, France, Sep. 2010.

[26] K. Zhou and D. Wang, “Relationship between space-vector modulation and three-phase carrier-based PWM: a comprehensive analysis,” *IEEE Transactions on Industrial Electronics*, vol. 49, no. 1, pp.186-196, Feb. 2002.

[27] A. M. Hava and N. O. Ćetin, “A generalized scalar PWM approach with easy implementation features for three-phase, three-wire voltage-source inverters,” *IEEE Transactions on Power Electronics*, vol. 26, no. 5, pp. 1385-1395, May 2011.

[28] Datasheet, Texas Instruments. [Online]. Available: http://www.ti.com/lit/ds/symlink/sn74abt541b.pdf

[29] Datasheet, Texas Instruments. [Online]. Available: http://www.ti.com/lit/ds/symlink/tlv5614.pdf

[30] H. Zhu, X. Xiao, and Y. D. Li, “Permanent magnet synchronous motor current ripple reduction with harmonic back-EMF compensation,” *International Conference on Electric Machines and Systems*, pp. 1094–1097, Incheon, South Korea , Oct. 2010.

Appendix: Main Interrupt Code

```
// MainISR
interrupt void MainISR(void)
{
// Verifying the ISR

    IsrTicker++;
    SPI_COUNTER++;

//  Connect inputs of the RMP module and call the ramp control macro
    if(lsw==0)   rc1.TargetValue = 0;
    else   rc1.TargetValue = SpeedRef;
    RC_MACRO(rc1)

//  Connect inputs of the RAMP GEN module and call the ramp generator macro
    rg1.Freq = rc1.SetpointValue;
    RG_MACRO(rg1)

//  Measure phase currents, subtract the offset and normalize into (-1,+1).
//  Connect inputs of the CLARKE module and call the clarke transformation macro

    clarke1.As=((AdcMirror.ADCRESULT1)*0.00024414-offsetA)*1.9339;
    clarke1.Bs=((AdcMirror.ADCRESULT2)*0.00024414-offsetB)*1.9325;

//    clarke1.Cs=((AdcMirror.ADCRESULT3)*0.00024414-offsetC)*2.12465;

//  Over-Current protection
    if ( _IQabs(clarke1.As)>I_lim || _IQabs(clarke1.Bs)>I_lim  ||
_IQabs(clarke1.Cs)>I_lim)
    GpioDataRegs.GPADAT.bit.GPIO26=0;

    CLARKE_MACRO(clarke1)

//    Call the QEP and speed calculation module
    QEP_MACRO(1,qep1);

    speed1.ElecTheta = qep1.ElecTheta;
    speed1.DirectionQep = (int32)(qep1.DirectionQep);
    SPEED_FR_MACRO(speed1)

    omega_e=speed1.SpeedRpm*PI*0.01666667*POLES;
    if (omega_e > omega_Ref)  speedFlag=1;
```

```
//  calculate the back-EMF and its harmonics compensation
   bemf1.Vdc=(AdcMirror.ADCRESULT4)*0.11352861-87.4225;
   bemf1.Angle=qep1.ElecTheta;
   bemf1.omega=omega_e;
   BEMF_COMP_MACRO(bemf1)

//  DC bus Voltage and Over-Speed protection
   if (bemf1.Vdc>300)  GpioDataRegs.GPADAT.bit.GPIO26=0;
   if (speed1.SpeedRpm>4000) GpioDataRegs.GPADAT.bit.GPIO26=0;

//  Connect inputs of the PARK module and call the park trans. macro
        park1.Alpha = clarke1.Alpha;
        park1.Beta = clarke1.Beta;

        if(lsw==0) park1.Angle = 0;
        else if(lsw==1) park1.Angle = rg1.Out;
        else park1.Angle = qep1.ElecTheta;

        park1.Sine = _IQsinPU(park1.Angle);
        park1.Cosine = _IQcosPU(park1.Angle);

        PARK_MACRO(park1)

//    Connect inputs of the PI module and call the PI dc bus voltage controller macro
        if (VdcRef>bemf1.Vdc*0.01)   VdcFlag=1;

        if (VdcFlag==0)  {pi_vdc.ui=0; pi_vdc.i1=0;}
        else
        {
        pi_vdc.Ref = VdcRef;
        pi_vdc.Fbk = bemf1.Vdc*0.01;
        PI_MACRO(pi_vdc);
        }

//    Connect inputs of the PI module and call the PI Modulation index controller
macro

        if (VdcFlag==0)  {pi_M.ui=0; pi_M.i1=IdRef;}
        else
        {
        pi_M.Ref = MRef;
        pi_M.Fbk = M;
        PI_MACRO(pi_M);
```

```
        }

//    Connect inputs of the PI module and call the PI speed controller macro
        if (SpeedLoopCount==SpeedLoopPrescaler)
          {
           pi_spd.Ref = rc1.SetpointValue;
           pi_spd.Fbk = speed1.Speed;
           PI_MACRO(pi_spd);
           SpeedLoopCount=1;
           }
        else SpeedLoopCount++;

        if(lsw==0 || lsw==1)    {pi_spd.ui=0; pi_spd.i1=0;}

//    Connect inputs of the PI module and call the PI IQ controller macro
        if(lsw==0)
        {
        pi_iq.Ref = 0;
        pi_id.Ref = _IQ(0.02);
        }

        else if(lsw==1)          // lsw=1 :  current close-loop control with fake position
angle
        {
         pi_iq.Ref = IqRef;
         pi_id.Ref = IdRef;
        }
        else if (GpioDataRegs.GPADAT.bit.GPIO22==1)   //lsw=2 and relay is turned
on: speed close-loop control with real position angle
        {
        pi_iq.Ref=pi_spd.Out;
        pi_id.Ref=IdRef;
        }
        else         // relay is shut down, dc bus voltage starts dropping
        {
            if (VdcFlag==0)   // When Vdc is still higher than command Vdc,
command zero iq
            {
            pi_iq.Ref=0;
            pi_id.Ref=IdRef;
            }
            else          // When Vdc drops below the command Vdc, command iq with
the Vdc PI
            {
```

```
                if (omega_e > omega_Ref)   // Before the speed drops below a safe
level, use the dc bus close-loop control to regulate command iq
                {
                pi_iq.Ref=pi_vdc.Out;
                pi_id.Ref=pi_M.Out;
                }

                else     // After the speed drops below omega_ref, gradually decrease
id* and iq* to zero
                {
                if (pi_iq.Ref<-0.0005)pi_iq.Ref=pi_iq.Ref+0.0005;
                if (pi_id.Ref<-0.0005)pi_id.Ref=pi_id.Ref+0.0005;
                if (pi_id.Fbk>-0.05) GpioDataRegs.GPADAT.bit.GPIO24=0;
                }
            }
        }

        pi_iq.Fbk = park1.Qs;
        pi_id.Fbk = park1.Ds;

        pi_id.Kp=0.6*pi_iq.Kp;
        pi_id.Ki=0.6*pi_iq.Ki;
        pi_id.Kdc=pi_iq.Kdc;

        pi_id.omega=omega_e;
        pi_iq.omega=omega_e;

        pi_iq.Error2=pi_id.Ref-pi_id.Fbk;   // import d-axis error for q-axis PI
calculation
        pi_id.Error2=pi_iq.Ref-pi_iq.Fbk;   // import q-axis error for d-axis PI
calculation

        pi_iq.Em=bemf1.Em;

        PI_Q_MACRO(pi_iq)
        PI_D_MACRO(pi_id)

// Calculate modulation index and Flag Over-modulation
        Vm=_IQmpy(pi_iq.Out,pi_iq.Out) + _IQmpy(pi_id.Out,pi_id.Out);
        M=_IQsqrt(Vm);

        if (M>1.1547) OMFlag=1;
        else          OMFlag=0;
```

```
//  Connect inputs of the INV_PARK module and call the inverse park trans. macro
        ipark1.Ds = pi_id.Out;
        ipark1.Qs = pi_iq.Out;
        ipark1.Sine=park1.Sine;
        ipark1.Cosine=park1.Cosine;
        IPARK_MACRO(ipark1)

//  Connect inputs of the SVGEN_DQ module and call the space-vector gen. macro
        svgen1.Ualpha = ipark1.Alpha;
        svgen1.Ubeta = ipark1.Beta;
        SVGENCOMM_MACRO(svgen1)

//  Connect inputs of the PWM_DRV module and call the PWM signal generation
macro
        pwm1.MfuncC1 = svgen1.Ta+bemf1.Eah;
        pwm1.MfuncC2 = svgen1.Tb+bemf1.Ebh;
        pwm1.MfuncC3 = svgen1.Tc+bemf1.Ech;
        PWM_MACRO(1,2,3,pwm1)                                          //

//    Connect inputs of the DATALOG module
            DlogCh1 = _IQtoQ15(pi_id.Fbk);
            DlogCh2 = _IQtoQ15(pi_id.ui);
            DlogCh3 = _IQtoQ15(pi_iq.Fbk);
            DlogCh4 = _IQtoQ15(pi_iq.ui);

//  SPI to DAC
switch(SPI_COUNTER)
{
case 1 : {SpiaRegs.SPITXBUF=4095*(6*pi_iq.Ref+6*0.1)+0x1000;}break;
case 2 : {SpiaRegs.SPITXBUF=4095*(6*pi_iq.Ref+6*0.1)+0x1000;}break;
case 3 : {SpiaRegs.SPITXBUF=4095*0.5*M+0x9000;}break;
case 4 : {SpiaRegs.SPITXBUF=4095*0.5*M+0x9000;SPI_COUNTER=0;}break;
}

//    Call the DATALOG update function.
   dlog.update(&dlog);

// Enable more interrupts from this timer
   EPwm1Regs.ETCLR.bit.INT = 1;

// Acknowledge interrupt to recieve more interrupts from PIE group 3
   PieCtrlRegs.PIEACK.all = PIEACK_GROUP3;

}   // MainISR Ends Here
```